Influence of Rotation on Fingering Convection in Planetary Cores

Martin Gray^a, Céline Guervilly^{a,*}, Graeme R. Sarson^a

^aSchool of Mathematics, Statistics and Physics, Newcastle University, Newcastle Upon Tyne, NE17RU, UK

Abstract

Stably stratified layers are thought to develop at the top of the liquid metallic cores of many terrestrial planets. We consider the case where the thermal gradient is stable but the compositional gradient is unstable, a situation particularly relevant to Mercury. The strong contrast between molecular diffusivities of temperature and composition leads to fingering convection. We investigate this process using hydrodynamical simulations in a rotating spherical shell, systematically varying the stratification strength N relative to the rotation rate Ω . In all regimes, the primary fingering mode forms narrow, elongated structures that shift orientation from the rotation axis to the direction of gravity as N^2/Ω^2 exceeds 10. The fingers remain laminar, with transverse scales proportional to thermal stratification but independent of rotation. Fingering convection also drives secondary large-scale flows across most of the explored parameter space, producing diverse dynamics including zonal flows, hemispherical convection, axisymmetric poloidal bands, finger clusters, and toroidal gyres. In the rapidly-rotating regime, laterally inhomogeneous mixing generates zonal flows in thermo-compositional wind balance; zonal flow direction and amplitude depend on N^2/Ω^2 , with amplitude weakening for strong stratification $N^2/\Omega^2 > 10$. In the intermediate regime $(N^2/\Omega^2 \sim 1)$, axisymmetric or spiraling poloidal bands emerge within the tangent cylinder, gradually overtaking the primary fingers. For stronger stratification, finger clusters and weak, large-scale density anomalies surrounded by toroidal gyres form in the upper domain. These diverse large-scale flows may interact with the dynamo-generated magnetic field in the deeper core, potentially influencing surface magnetic fields.

1. Introduction

Mercury possesses a surface magnetic field that is weak, dominantly dipolar, and unusually axisymmetric, with a significant northward offset of the magnetic equator (Anderson et al., 2012). These characteristics are difficult to reconcile with conventional convective dynamo models, which typically predict stronger fields with significant non-axisymmetric components (Christensen, 2006). One leading explanation invokes the presence of a stably stratified layer at the top of Mercury's liquid outer core, which would suppress radial convective motions whilst allowing differential rotation, thereby modifying the dynamo-generated field before it reaches the surface (Christensen, 2006; Christensen and Wicht, 2008; Stanley and Mohammadi, 2008; Manglik et al., 2010; Vilim et al., 2010; Wicht and Heyner, 2014; Tian et al., 2015; Takahashi et al., 2019; Kolhey et al., 2025).

Thermal evolution models incorporating geophysical constraints support the existence of such a stable layer in Mercury (Dumberry and Rivoldini, 2015; Davies et al., 2024; Knibbe et al., 2025). This stratification is thought to result from a sub-adiabatic heat flux across the core—mantle boundary, possibly in combination with a destabilising composition gradient due to the upwards release of a fluid enriched in light elements from the inner core solidification or from an underlying iron-snow layer (Dumberry and Rivoldini, 2015). The resulting configuration (thermally stable but compositionally unstable) is conducive to double-diffusive instabilities that drive fingering convection (Radko, 2013). The assumption that radial convective flows are largely suppressed in the stable layer may therefore be invalid, calling into question the influence of the stable layer on the dynamo field. The presence of fingering convection in the stable layer could have significant consequences for the morphology of Mercury's observed magnetic field. However, the interaction between fingering convection and magnetic fields is largely unknown (Harrington and Garaud, 2019;

^{*}corresponding author: celine.guervilly@ncl.ac.uk

Fraser et al., 2024): it may amplify the field or weaken it through local cancellations or enhanced turbulent diffusion. Associated differential rotation could suppress non-axisymmetric components, and explain the observed axisymmetry and hemispheric asymmetry of the field (Christensen and Wicht, 2008; Stanley and Mohammadi, 2008; Kolhey et al., 2025).

Fingering convection occurs when a stabilising thermal gradient is opposed by an unstable compositional gradient, and where thermal diffusivity greatly exceeds compositional diffusivity (Stern, 1960). The potential energy linked to the destabilising composition is released through the rapid molecular diffusion of temperature. This process drives vertical motions that can greatly enhance the transport of heat and chemical composition in otherwise stable layers (Traxler et al., 2011a; Stellmach et al., 2011). Fingering convection has been widely explored in fields such as oceanography (Schmitt, 1994; Kunze, 2003), magma dynamics (Sparks et al., 1984; Hansen and Yuen, 1990), and stellar interior dynamics (Garaud, 2021). The potential for fingering convection to operate in the metallic cores of planets has recently received increasing attention (Manglik et al., 2010; Net et al., 2012; Bouffard et al., 2017; Monville et al., 2019; Silva et al., 2019; Mather and Simitev, 2021; Guervilly, 2022; Tassin et al., 2024). A key distinction between these different natural systems lies in the value of the Prandtl number (Pr), which quantifies the ratio of kinematic viscosity to thermal diffusivity. While oceans and magmas typically have Pr > 1, liquid metals such as those found in planetary cores exhibit lower values, on the order of $Pr \sim 0.1$. Studies of fingering convection in stellar interiors, where $Pr \ll 1$, have demonstrated that the Prandtl number plays a critical role in controlling the dynamics (Garaud, 2018), thereby limiting the direct applicability of results across different natural systems. One notable example is the near-absence of thermo-compositional staircases at low Prandtl numbers (Traxler et al., 2011b; Brown et al., 2013). These staircases, which consist of well-mixed layers separated by sharp stratified interfaces, are known to substantially enhance mixing efficiency when present at high Prandtl numbers (e.g. Stellmach et al., 2011).

The objective of this study is to characterise the dynamics of fingering convection under conditions relevant to metallic cores. The study focuses on thick stable layers, particularly suitable for Mercury, but thermally-stratified regions in liquid outer cores are also relevant for the Earth (e.g. Greenwood et al., 2021) and Ganymede (Hauck et al., 2006). This work builds on recent studies by Guervilly (2022) and Tassin et al. (2024), both of which explore fingering convection in spherical shell geometries across wide regions of parameter space. Tassin et al. (2024) investigates the non-rotating regime, while Guervilly (2022) considers the regime where rotational effects dominate over stratification (a regime that we will quantify below). In the latter case, at low forcing (i.e. small Rayleigh numbers), the flow organises into tall, columnar structures aligned with the rotation axis, with azimuthal size comparable to the layer thickness (Monville et al., 2019; Mather and Simitev, 2021). As the forcing increases, these structures become increasingly sheet-like and thin in azimuth while remaining axially elongated. Radial motions remain largely laminar, and strong equatorially-symmetric zonal (i.e. axisymmetric and azimuthal) flows develop, eventually dominating the non-axisymmetric flow. In contrast, in the absence of rotation, Tassin et al. (2024) finds that the fingers align radially. Tassin et al. further examines how thermal and compositional fluxes, velocities, and finger sizes scale with key dimensionless parameters, deriving new scaling laws. Additionally, they identify a secondary instability characterised by the formation of large-scale toroidal jets that distort the fingering structures and induce relaxation oscillations. Given the uncertainty surrounding the stratification strength in Mercury's stable layer, the present study aims to bridge the gap between the strongly-stratified, non-rotating regime of Tassin et al. (2024) and the weakly-stratified, rapidly-rotating regime of Guervilly (2022). We focus specifically on identifying the conditions under which the transition between these regimes occurs. As a first step in addressing this complex problem, magnetic fields are neglected in the present

The paper is structured as follows. Section 2 presents the mathematical and computational formulation of the model. Section 3 details the results, including the dynamics across weak, intermediate, and rapid rotation regimes, the emergence of differential rotation (i.e. zonal flows), and the efficiency of convective transport. Concluding remarks are provided in Section 4.

2. Model

2.1. Governing equations

We model a stably-stratified layer of Boussinesq fluid confined within a spherical shell. The inner boundary, at radius R_i , represents the interface with the deeper convective core, while the outer boundary, at radius R_o , corresponds

to the core-mantle boundary. The thickness of the stable layer at the top of Mercury's core is not well constrained by thermal evolution models. Here we model a thick layer of depth 800 km, which is at the upper end of the proposed range (Wardinski et al., 2021; Davies et al., 2024). This corresponds to an aspect ratio of $\chi = R_i/R_o = 0.6$.

The fluid layer rotates about the z-axis with rotation rate Ω . Gravity is directed radially inward and varies linearly with spherical radius r, given by $\mathbf{g} = -g_0 r/R_o \mathbf{e}_r$ where g_0 is a constant. The fluid has constant viscosity ν , thermal diffusivity κ_t and compositional diffusivity with $\kappa_t > \nu > \kappa_c$.

The density ρ depends linearly on the temperature T and the composition C (i.e. the concentration in light elements) of the Boussinesq fluid:

$$\frac{\rho}{\rho_m} = 1 - \alpha_t (T - T_m) - \alpha_c (C - C_m),\tag{1}$$

where α_t is the coefficient of thermal expansion, and α_c the compositional analogue to α_t , with constant α_t , $\alpha_c > 0$. The subscript m denotes a constant mean value. The temperature and composition are decomposed into a constant mean, a static profile (denoted by the subscript s) and a perturbation:

$$T(r,\theta,\phi,t) = T_m + T_s(r) + \Theta(r,\theta,\phi,t), \tag{2}$$

$$C(r,\theta,\phi,t) = C_m + C_s(r) + \xi(r,\theta,\phi,t), \tag{3}$$

in spherical polar coordinates (r, θ, ϕ) and where t is time.

The equations are nondimensionalised using the layer thickness $D = R_o - R_i$ as a unit for lengths, D^2/ν for times, $\nu^2/\alpha_t g_o D^3$ for temperature, and $\nu^2/\alpha_c g_o D^3$ for composition. The dimensionless inner and outer radii are thus $r_i = R_i/D = 1.5$ and $r_o = R_o/D = 2.5$. The dimensionless governing equations are

$$\frac{\partial \mathbf{u}}{\partial t} + (\mathbf{u} \cdot \nabla)\mathbf{u} + \frac{2}{Ek}\mathbf{e}_z \times \mathbf{u} = -\nabla p + \nabla^2 \mathbf{u} + (\Theta + \xi)\frac{r}{r_o}\mathbf{e}_r, \tag{4}$$

$$\frac{\partial \Theta}{\partial t} + \mathbf{u} \cdot \nabla \Theta + u_r \frac{\mathrm{d}T_s}{\mathrm{d}r} = \frac{1}{Pr} \nabla^2 \Theta, \tag{5}$$

$$\frac{\partial \xi}{\partial t} + \mathbf{u} \cdot \nabla \xi + u_r \frac{\mathrm{d}C_s}{\mathrm{d}r} = \frac{1}{Sc} \nabla^2 \xi, \tag{6}$$

where $\mathbf{u} = (u_r, u_\theta, u_\phi)$ is the solenoidal velocity and p the pressure. The dimensionless numbers are the Ekman, Prandtl, and Schmidt numbers defined respectively as

$$Ek = \frac{v}{\Omega D^2}, \quad Pr = \frac{v}{\kappa_t}, \quad Sc = \frac{v}{\kappa_c}.$$
 (7)

The radial gradients of the static fields are obtained by solving the diffusion equations in the absence of motions. At the inner boundary, the static temperature and composition gradients are imposed:

$$T'_{s}(r_{i}) = \frac{dT_{s}}{dr}\Big|_{r_{i}} = -\frac{Ra_{t}}{Pr}\frac{1}{r_{i}}, \quad C'_{s}(r_{i}) = \frac{dC_{s}}{dr}\Big|_{r_{i}} = -\frac{Ra_{c}}{Sc}\frac{1}{r_{i}}, \tag{8}$$

where the Rayleigh numbers are dimensionless numbers defined as

$$Ra_t = \frac{\alpha_t g_o q_i R_i D^3}{\nu \kappa_t}, \quad Ra_c = \frac{\alpha_c g_o f_i R_i D^3}{\nu \kappa_c}, \tag{9}$$

where $q_i \propto -T_s'(r_i)$ and $f_i \propto -C_s'(r_i)$ are the dimensional static temperature and composition fluxes at the inner boundary. In fingering convection, the static temperature gradient through the layer is stable while the static compositional gradient is unstable, so $q_i < 0$ and $f_i > 0$, and so $Ra_t < 0$ and $Ra_c > 0$. At the core-mantle boundary, we assume that there is no flux of light elements to/from the mantle, hence $C_s'(r_o) = 0$. We therefore include a sink term in the diffusion equation for C_s to compensate the inflow of light elements at the inner boundary and achieve a steady state (see further detail in Guervilly (2022)). For the static temperature, the outward heat flux integrated over the spherical surface at r_o equals the incoming heat flux integrated over the spherical surface at r_i to ensure a steady state, so no

source term are included in the diffusion equation for T_s . The gradient of the static fields in the domain are thus

$$T_s' = \frac{\mathrm{d}T_s}{\mathrm{d}r} = -\frac{Ra_t}{Pr} \frac{r_i}{r^2},\tag{10}$$

$$C_s' = \frac{\mathrm{d}C_s}{\mathrm{d}r} = \frac{Ra_c}{Sc(1-\chi^3)} \left(\frac{r_i}{r_o^3}r - \frac{r_i}{r^2}\right). \tag{11}$$

The boundary conditions for the perturbations are zero radial fluxes at $r = r_i$ and $r = r_o$,

$$\frac{\partial \Theta}{\partial r}\Big|_{r_i} = \frac{\partial \xi}{\partial r}\Big|_{r_i} = \frac{\partial \Theta}{\partial r}\Big|_{r_o} = \frac{\partial \xi}{\partial r}\Big|_{r_o} = 0.$$
 (12)

We neglect any dynamical interaction with the deep convective core at $r = r_i$ for simplicity. We therefore use impenetrable boundary conditions at $r = r_i$ and $r = r_o$. We use stress-free boundary conditions at $r = r_i$ to model the interface with the convective liquid core and no-slip boundary conditions at $r = r_o$ to model the rigid core-mantle boundary.

The diffusivity coefficients are held constant throughout this study. Following Monville et al. (2019); Guervilly (2022), we adopt a Prandtl number of Pr = 0.3 and a Schmidt number of Sc = 3, which yields a Lewis number $Le = \kappa_t/\kappa_c = Sc/Pr = 10$ for all simulations. Although this value is lower than that expected in planetary cores ($Le = O(10^3)$), it remains computationally tractable and allows for a meaningful exploration of double-diffusive fingering instabilities within a relevant parameter regime as described below.

2.2. Stratification and domain of fingering convection

The stratification of the layer measures the stability of the fluid to vertical displacements. It is quantified by the buoyancy frequency N, also called the Brunt-Väisälä frequency, which corresponds to the frequency of oscillations of a vertically-displaced fluid parcel under the restoring force of gravity. N^2 is proportional to minus the radial density gradient, so in a stably-stratified layer, where the density decreases with radius, $N^2 > 0$. The system is unstably stratified when $N^2 < 0$. We measure the buoyancy frequency from the static profiles (10)-(11), which gives in dimensionless units,

$$\tilde{N}^2 = \frac{N^2}{v^2/D^4} = \frac{r}{r_o} \left(T_s' + C_s' \right). \tag{13}$$

For our choice of static gradients, N^2 varies slightly with radius, with the stratification being strongest at the bottom of the layer and $N^2(r_o) = 0.85N^2(r_i)$. In the rest of the paper, values of N^2 will always be quoted at $r = r_i$.

In a rotating domain, it is convenient to measure N relative to the rotation rate Ω :

$$\frac{N^2}{\Omega^2} = -\frac{Ek^2}{r_0} \left(\frac{Ra_t}{Pr} + \frac{Ra_c}{Sc} \right) = \frac{Ek^2}{r_0} \frac{Ra_c}{Sc} \left(R_\rho^i - 1 \right), \tag{14}$$

where the density ratio R_{ρ} is

$$R_{\rho} = \frac{|T_{s}'|}{|C_{s}'|}, \quad R_{\rho}^{i} = R_{\rho}(r_{i}) = \frac{|Ra_{t}|Le}{Ra_{c}}.$$
 (15)

Double-diffusive instabilities are commonly characterised by the density ratio, which delineates the conditions under which they may arise. In non-rotating, planar layers with uniform static gradients, the system becomes linearly unstable to the double-diffusive fingering instabilities when

$$1 < R_{\rho} < Le, \tag{16}$$

assuming $Le \gg 1$ and sufficiently high Rayleigh numbers (Stern, 1960; Baines and Gill, 1969). Values of $R_{\rho} < 1$ correspond to unstably-stratified systems with $N^2 < 0$. Rotational effects do not significantly alter this critical range for large Ra_c (Sengupta and Garaud, 2018; Monville et al., 2019). However, in spherical geometry with rotation, large-scale double-diffusive modes with low azimuthal wavenumber can be preferred to small-scale fingers near the stability boundaries, especially for small Ra_c (Silva et al., 2019; Monville et al., 2019; Guervilly, 2022). Fingering convection can also be preferred for $R_{\rho} < 1$ (Hage and Tilgner, 2010; Schmitt, 2011; Kellner and Tilgner, 2014; Yang

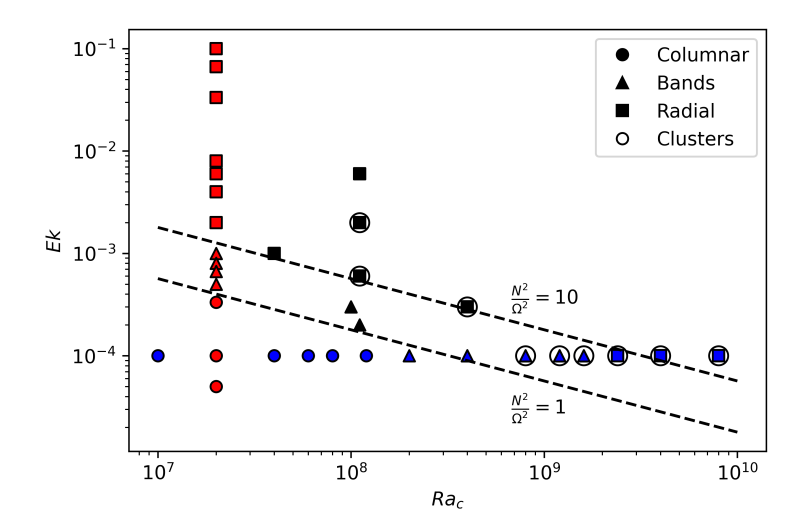


Figure 1: Simulations in the parameter space $Ek - Ra_c$. All the simulations were performed with Le = 10, Pr = 0.3 and $R_\rho^i = Le/3$. The lower (upper) dashed line represents $N^2/\Omega^2 = 1$ ($N^2/\Omega^2 = 10$ respectively). Series 1 simulations are represented in red and Series 2 simulations in blue. Columnar/radial/bands refer to the structure of the radial flows in the rapidly-rotating/weakly-rotating/intermediate regimes. The location of the finger clusters (§3.2.2) is indicated by large open circles.

et al., 2015). Since $Le \gg 1$ in planetary cores, the parameter regime prone to fingering instability is therefore broad, suggesting that fingering convection may play a role across a wide range of thermal and compositional stratifications. In our study, R_{ρ} increases with radius (see Figure 2 in Guervilly (2022)). At the bottom of the domain, the unstable range (16) corresponds to

$$Ra_c/Le < |Ra_t| < Ra_c. \tag{17}$$

The density ratio goes to infinity at the outer boundary as C_s' is zero there. R_ρ crosses the theoretical onset of fingering convection for $R_\rho(r=r_s)=Le$. This implies that, while the bottom of the domain might be prone to fingering instabilities, the top of the domain might not be. As the radial profile of R_ρ depends on $|Ra_t|/Ra_c$ (and not on Ra_t or Ra_c individually), fixing this ratio leaves radius r_s unchanged. In this study, we fix $Ra_t = -Ra_c/3$ i.e. $R_\rho^i = Le/3$. This implies that $r_s = 2.26$, so we would expect fingering convection to occur in the inner 76% of the radial domain at large Rayleigh numbers.

2.3. Numerical method

All the simulations are performed with the open-source code XSHELLS (Schaeffer, 2013; Schaeffer et al., 2017). XSHELLS is a C++ pseudo-spectral code that solves the governing equations (4)-(6) in a 3D spherical geometry. To ensure that the velocity field is solenoidal, \mathbf{u} is decomposed into poloidal and toroidal scalars, U_p and U_t ,

$$\mathbf{u} = \nabla \times \nabla (U_{n}\mathbf{r}) + \nabla \times (U_{t}\mathbf{r}),$$

where r is the position vector. All the scalars $(U_p, U_t, \Theta \text{ and } \xi)$ are expanded in spherical harmonics $Y_l^m(\theta, \phi)$ of degree l and order m, which are truncated at L_{max} and M_{max} respectively. In the radial direction, the code uses a second-order finite difference scheme with N_r points. The code uses a second-order time-stepping scheme with an implicit treatment of the diffusive terms and explicit treatment of the non-linear terms. Details of the numerical resolution used for each simulation are provided in Appendix A.

3. Results

3.1. Overview

3.1.1. Parameter survey

We first give an overview of the results before describing the flow in the different dynamical regimes in later sections. All the simulations were run at a constant density ratio $R_{\rho}^{i} = Le/3$. As shown in Figure 1, the ratio N^{2}/Ω^{2}

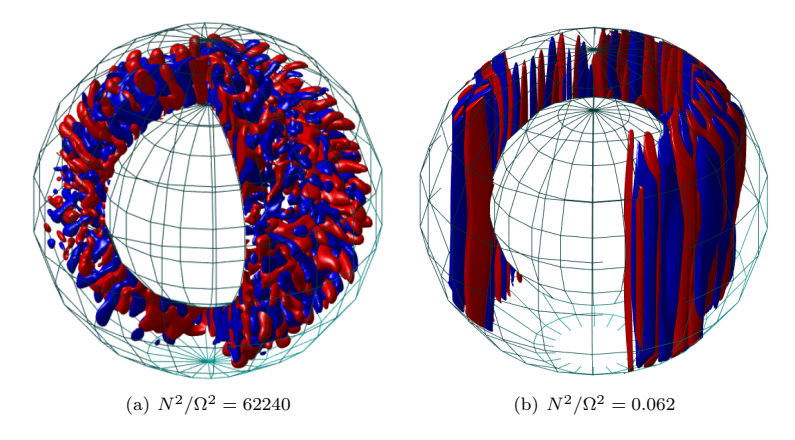


Figure 2: Isosurfaces of the radial velocity for two representative cases of (a) $N^2/\Omega^2 \gg 1$ ($Ek = 10^{-1}$ in Series 1) and (b) $N^2/\Omega^2 \ll 1$ ($Ek = 10^{-4}$ in Series 1). Red (blue) indicates positive (negative) values of u_r and the isosurfaces corresponds to 10% of the maximum values of u_r in a given snapshot.

is varied in two ways: (1) varying Ekman number at fixed Rayleigh number ($Ra_c = 2 \times 10^7$) (Series 1); (2) varying Rayleigh numbers (i.e. varying Ra_c and Ra_t by the same factor to maintain constant R_ρ^i) at fixed Ekman number ($Ek = 10^{-4}$) (Series 2). Tables A.1 and A.2 in Appendix A list the input parameters and numerical resolutions of all the simulations. The range of the dynamical lengthscales increases with the Rayleigh numbers, implying that the exploration of the regime $N^2/\Omega^2 \gg 1$ is more computationally demanding in Series 2 and, consequently, restricted to $N^2/\Omega^2 \lesssim 25$. For convenience, we define the weakly-rotating regime as $N^2/\Omega^2 > O(1)$, understood to be relative to the strength of the stratification. Conversely, we refer to $N^2/\Omega^2 < O(1)$ as the rapidly-rotating regime.

Two cases representative of $N^2/\Omega^2 \gg 1$ and $N^2/\Omega^2 \ll 1$ are illustrated in Figure 2, which show snapshots of the isosurfaces of the radial velocity. Comparison of the two cases show one immediate difference: whilst the structure of the radial velocity in the weakly-rotating case is essentially aligned with gravity ("radial" fingers), it is aligned with the rotation axis in the rapidly-rotating case ("columnar" fingers). In both cases, the fingers do not occupy the whole volume of the sphere: the density ratio increases with radius in our system so the fingers develop preferentially close to the inner boundary. Additionally, fingering convection within the tangent cylinder is inhibited for rapid rotation, and only sets in at higher values of N^2/Ω^2 . This is due to the detrimental effect of rotation on the buoyancy-driven instability, which is particularly pronounced when the rotation axis is aligned with gravity, similar to the behaviour observed in single-component overturning convection (e.g. Gastine and Aurnou, 2023). Fingering convection can occur inside the tangent cylinder for $N^2/\Omega^2 < 1$ as shown in Section §3.3.

3.1.2. Finger scale

In the weakly- and rapidly-rotating regimes, the fingers have a specific lengthscale in the transverse direction (i.e. the direction tangential to the rotation axis for rapid rotation and to the radial direction for weak rotation). In non-rotating plane layer, the fingering instability develops as elongated fingers with a transverse lengthscale that follows the dimensionless "Stern scale" $\mathcal{L}_{theo} = (|Ra_t|/r_o)^{-1/4}$ for large Rayleigh numbers and when $1 \ll R_\rho \ll Le$ (Stern, 1960; Schmitt, 1979). In spherical shell simulations without rotation, Tassin et al. (2024) found that the observed transverse finger scale closely follows the Stern scale's dependence on Ra_t , although it also exhibits sensitivity to the density ratio. In the rapidly-rotating regime, Guervilly (2022) demonstrated that, at a fixed density ratio and sufficiently large Rayleigh numbers, the transverse finger scale remains well described by the Stern scale across varying Ekman numbers. This suggests that, for $N^2/\Omega^2 < 1$, rotation does not significantly influence the transverse finger scale.

To measure a typical transverse finger scale, we estimate the most energetic scale of the poloidal flow from the power spectra of the poloidal kinetic energy in Series 1 and 2 cases (Figure 3). In Series 1, where Ra_t is held constant, the spectra exhibit a well-defined peak for both $N^2/\Omega^2 < 1$ and $N^2/\Omega^2 > 1$. In both cases, the peak occurs at approximately the same wavenumber, consistent with the Stern scale, indicating that it is largely insensitive to variations in Ek. The most noticeable difference is that length scales at or above the Stern scale are more energetic for $N^2/\Omega^2 > 1$. In Series 2, where Ra_t increases, a well-defined spectral peak is again observed for both $N^2/\Omega^2 < 1$ and

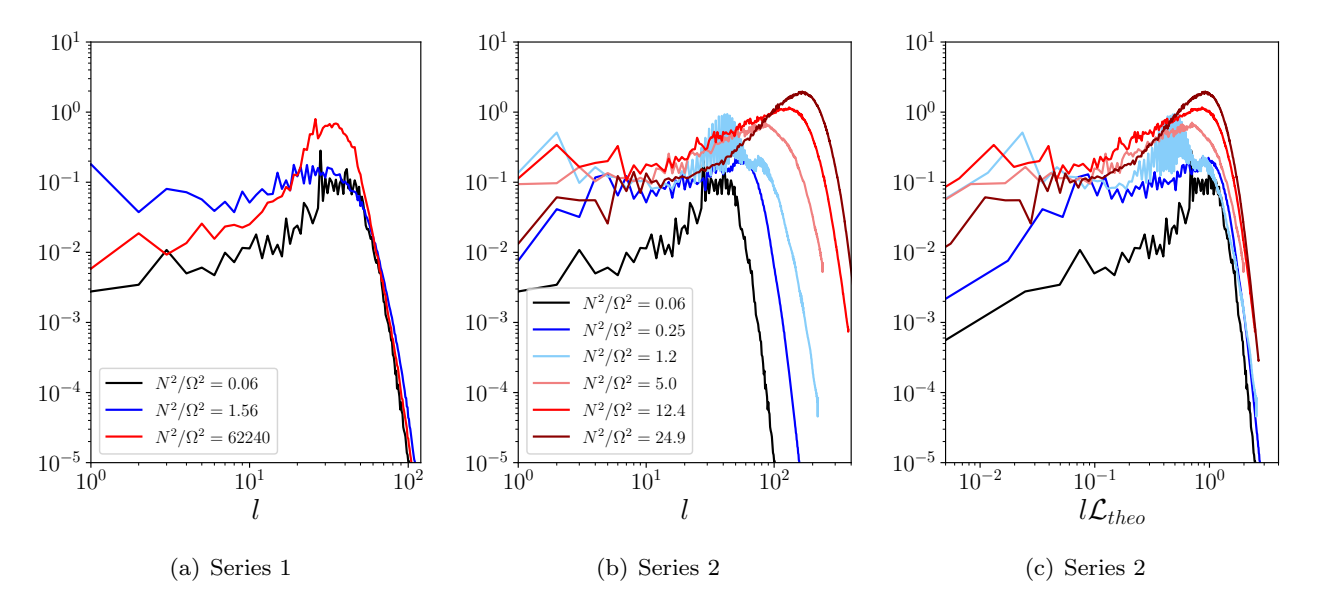


Figure 3: Spectra of the poloidal kinetic energy as a function of the spherical harmonics degree l for selected cases in Series 1 and 2 in (a)-(b). The spectra are calculated from a snapshot and averaged in radius excluding the boundary layers. In (c), the degree l is normalised by $\mathcal{L}_{theo} = (|Ra_l|/r_o)^{-1/4}$. $N^2/\Omega^2 = 0.06$ has the same parameters in both Series.

 $N^2/\Omega^2 > 1$. As N^2/Ω^2 increases, the flow becomes more energetic across all scales. When the spherical harmonics degree l is normalised by \mathcal{L}_{theo} on the x-axis (Figure 3c), the spectral peaks align, indicating consistency with the predicted scaling. The spectral peak occurs at a spherical harmonics degree $l_{peak} \approx 1/\mathcal{L}_{theo}$, corresponding to a lengthscale $\mathcal{L} = \pi r_i/l_{peak} \approx 5\mathcal{L}_{theo}$ for the transverse finger size. In summary, the transverse scale of both columnar and radial fingers follows the Stern scale in our simulations with fixed density ratio. The intermediate regime is visibly different: in Series 1, the spectrum displays a flat slope at low wavenumbers up to the Stern scale; in Series 2, two separate spectral peaks emerge: one at the Stern scale and another at approximately half that wavenumber. Section §3.4 will explore this novel feature.

3.1.3. Scaling of the radial velocity

To evaluate how the radial variation of R_{ρ} influences the vigour of fingering convection throughout the layer, Figure 4 shows the radial profile of the root mean square (r.m.s.) radial velocity for increasing values of N^2/Ω^2 . In all cases, radial motions are strongest near the bottom of the layer, just outside the lower boundary layer, and decrease monotonically with radius. Only weak radial flows are observed to cross the upper region beyond $r > r_s$ (where $R_{\rho}(r = r_s) = Le$).

To determine how the mean velocity amplitude scales with the parameters, Figure 5(a) shows the variation of the Reynolds number as a function of N^2/Ω^2 . The Reynolds number Re is a dimensionless measure of the r.m.s. poloidal velocity V_p ,

$$Re = \frac{V_p D}{v},\tag{18}$$

where V_p is calculated from the volume and time average of the poloidal kinetic energy. In Series 1, Re remains relatively constant for $N^2/\Omega^2 \le 1$. The cases with $N^2/\Omega^2 < 0.1$ appear as outliers as they exhibit no flow within the tangent cylinder. However, when Re is rescaled by the fraction of the volume outside the tangent cylinder relative to the total layer volume (represented by triangles in Figure 5), these points align more closely with the others in the same regime. For $N^2/\Omega^2 > 1$, Re increases up to $N^2/\Omega^2 \approx 100$, beyond which it plateaus. This saturation suggests that rotational effects become dynamically negligible at high N^2/Ω^2 in Series 1, i.e. as $Ek \to 0$ (this would not necessarily be true for Series 2). In Series 2, Re consistently increases with N^2/Ω^2 , with a noticeable transition near $N^2/\Omega^2 \approx 1$, beyond which Re increases more steeply.

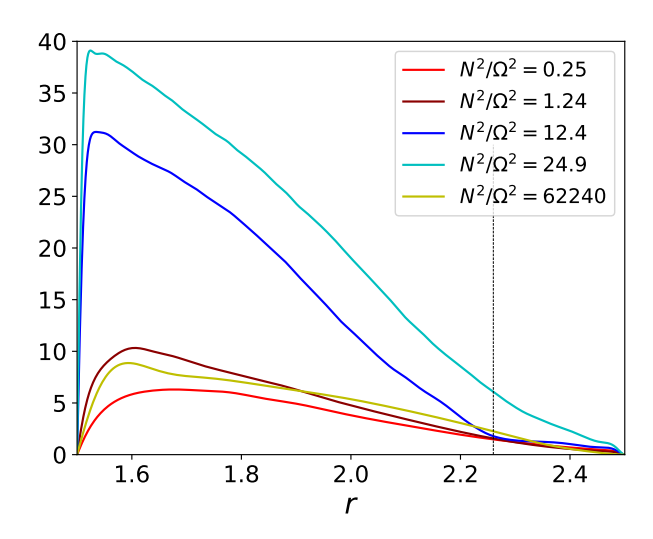


Figure 4: Radial profile of the r.m.s. radial velocity for selected simulations in Series 2 (0.25 $\leq N^2/\Omega^2 \leq$ 24.9) and Series 1 ($N^2/\Omega^2 =$ 62240). The vertical dashed line corresponds to the radius r_s where $R_\rho(r=r_s)=Le$.

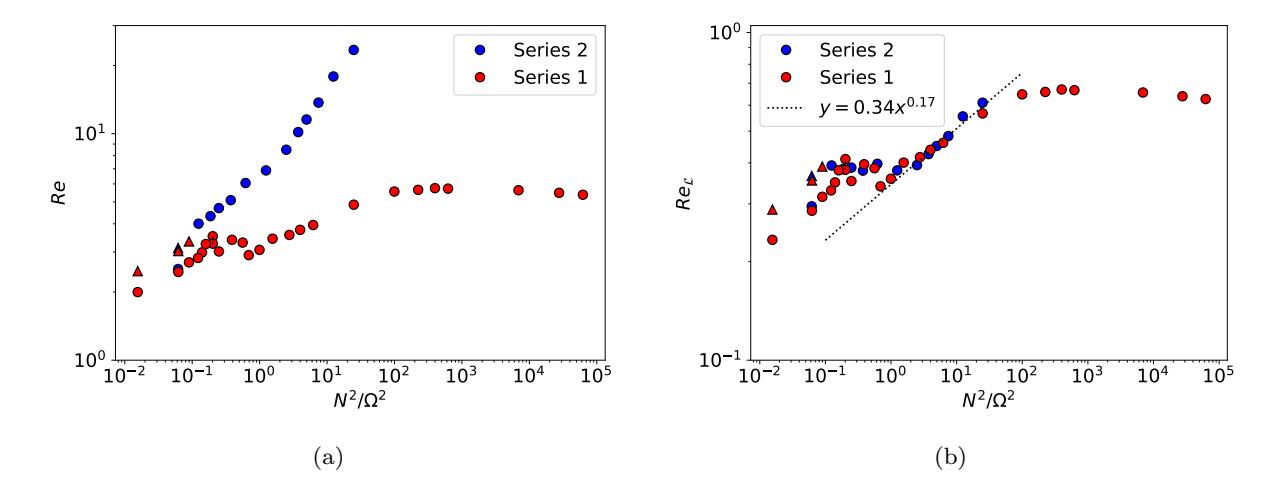


Figure 5: Variation of (a) the Reynolds number Re and (b) the local Reynolds number $Re_{\mathcal{L}}$ as a function of N^2/Ω^2 . Both Reynolds numbers are based on the mean poloidal velocity. The triangles corresponds to the rescaled Reynolds number where fingering convection occurs only outside the tangent cylinder for $N^2/\Omega^2 < 0.1$. The case $N^2/\Omega^2 = 0.2$ of Series 1 is represented by two values (linked by a dotted line) corresponding to two states of the zonal flow (see §3.5).

The variation of Re with N^2/Ω^2 indicates the presence of successive power-law relations, which we can compare with the theoretical scalings that have been proposed in non-rotating (e.g. Brown et al., 2013; Yang et al., 2016; Hage and Tilgner, 2010; Tassin et al., 2024) and rotating fingering convection (Sengupta and Garaud, 2018) for regimes of weakly and strongly driven fingering convection, defined by the reduced density ratio (Traxler et al., 2011a):

$$r_{\rho} = \frac{R_{\rho}^{i} - 1}{Le - 1}. (19)$$

The regime of weakly driven convection corresponds to $r_{\rho} \approx 1$ (i.e. close to the linear onset for large Rayleigh numbers, $R_{\rho}^{i} \approx Le$), whilst the regime of strongly-driven fingering convection, close to neutral stability ($R_{\rho}^{i} = 1$), corresponds to $0 < r_{\rho} \ll 1$. Note that here $r_{\rho} = 0.26$, so our simulations have moderate driving by that definition. Nevertheless, we can attempt to compare our numerical data to theoretical scalings proposed for $r_{\rho} \ll 1$.

A simple theoretical scaling can be derived by assuming that the timescale for thermal diffusion and advection are similar at the finger scale \mathcal{L} , meaning that the typical radial velocity of the fingers is of the order of κ_t/\mathcal{L} , i.e. the local Péclet number is constant (Radko, 2013):

$$Re_{\mathcal{L}} = Re\mathcal{L} \sim \frac{1}{Pr}.$$
 (20)

However, for small Prandtl numbers, Brown et al. (2013) and Sengupta and Garaud (2018) argue that the saturation of the fingering instability is caused by a secondary shear instability of the fingers (Radko and Smith, 2012) and propose an alternative scaling depending on r_{ρ} . In particular, for the range of parameters that is closest to our study, $r_{\rho} \ll Pr < 1$ and $Le \gg 1$, Brown et al. (2013) found that

$$Re_{\mathcal{L}} \sim \frac{1}{Pr^{1/2}}.$$
 (21)

For $N^2/\Omega^2 \lesssim 1$, Monville et al. (2019) and Guervilly (2022) found that the local Reynolds number remains approximately constant. These studies cannot distinguish between the two scalings (20) and (21) since the Prandtl number is fixed and not particularly small (Pr = 0.3). Similarly, in this study, R_ρ^i (or r_ρ), Pr and Sc are fixed, so we can only test the dependence of Re on one of the Rayleigh numbers.

Figure 5(b) shows the local Reynolds number, $Re_{\mathcal{L}} = Re\mathcal{L}$ where $\mathcal{L} = \mathcal{L}_{theo}\pi r_i$ (and $\mathcal{L}_{theo} = (|Ra_t|/r_o)^{-1/4}$ as above), as a function of N^2/Ω^2 . First we note that the local Reynolds numbers are always below one, meaning that, at the finger scale, the poloidal flow remains laminar. For $N^2/\Omega^2 < 1$, the local Reynolds number remains constant for both Series. Since the Rayleigh numbers are kept fixed in Series 1 and the transverse finger length is unaffected by rotation, a constant $Re_{\mathcal{L}}$ explains the constant Re for $N^2/\Omega^2 < 1$ in Figure 5(a). The critical value of Ra_c at the onset of fingering convection, Ra_c^{crit} , varies as $Ra_c^{crit} \propto Ek^{-1}$ for $Ek \ll 1$ (Monville et al., 2019), so it is worth noting that the increase of the supercriticality $Ra_c/Ra_c^{crit} \sim Ra_cEk$ in Series 1 does not affect the Reynolds number in that regime. By contrast, for $N^2/\Omega^2 > 1$, the local Reynolds number increases before reaching the plateau of $N^2/\Omega^2 > 100$. In the range $2 \le N^2/\Omega^2 \le 30$, the best fit to a power law for both Series is $Re_{\mathcal{L}} \sim (N^2/\Omega^2)^{0.17}$. Tassin et al. (2024) proposed a theoretical scaling for non-rotating fingering convection at $r_\rho \ll 1$,

$$Re \sim Ra_c^{2/3}|Ra_t|^{-1/4}Sc^{-1},$$
 (22)

which can be re-written as

$$Re_{\mathcal{L}} = Re\mathcal{L} \sim Ra_c^{1/6} R_o^{-1/2} P r^{-1/2} S c^{-1/2},$$
 (23)

where we used again $\mathcal{L} \propto |Ra_t|^{-1/4}$. Tassin et al. found a good agreement between their data, those of Yang et al. (2016) and this theoretical scaling. Noting that N^2/Ω^2 varies as Ra_c for fixed R_ρ (equation (14)), the 0.17 exponent from our best fit also supports the dependence on $Ra_c^{1/6}$ in Series 2. Note that the theoretical scaling (22) assumes a 1/3 power law dependence of the compositional Nusselt on Ra_c , which is only partly in agreement with our simulation data in that range (see §3.6 below). Remarkably, Series 1 also closely follows the scaling $(N^2/\Omega^2)^{1/6}$ (i.e. $Re_{\mathcal{L}} \sim Ek^{1/3}$) in the interval $2 \leq N^2/\Omega^2 \leq 30$. This is unexplained by the scaling (22), which is derived for non-rotating systems. The increased supercriticality Ra_c/Ra_c^{crit} with Ek in Series 1 could partially explain the increase in the local Reynolds number, although a shallower slope $Re \sim Ek^{1/6}$ would be expected if $Re_{\mathcal{L}}$ only depended on the supercriticality.

In the following, we will briefly describe the flows in the weakly- and rapidly-rotating regimes (§3.2 and 3.3) before presenting the intermediate regime in more detail (§3.4). Section 3.5 presents the formation and saturation of the axisymmetric and azimuthal (i.e. zonal) flows. In Section 3.6, we discuss the transport properties of the fingering convection in the different regimes.

3.2. Weak rotation

3.2.1. Radial fingers

Figure 6 shows the radial velocity projected on a spherical surface at r=1.8 for simulations in Series 1 and 2 representative of the weakly-rotating regime with $N^2/\Omega^2 > 1$. Since the thermal stratification is significantly stronger for our chosen case from Series 2 (Ra_t is 400 times larger), the finger size is visibly smaller. In either cases, no noticeable difference in the radial flows of the equatorial and polar regions is visible, suggesting that the dynamics of the fingers are weakly influenced by rotation. The meridional slices of u_r in Figure 6 shows that, as expected from the radial profiles in Figure 4, the radial fingers are preferentially located in the inner region where the density ratio is smallest. Similarly to the radial fingers described in Tassin et al. (2024) in the absence of rotation, the fat fingers at low Ra_c (Series 1) are tubular structures with a radial lengthscale that extend over more than half of the layer depth, whilst at larger Ra_c (Series 2), the thin fingers have undulating structures with shorter radial lengthscale.

The spherical projections of u_r in Figure 6 (especially in Series 1) show an asymmetry in the distribution of the upward and downward flows, with concentrated upflows amongst more dilute downflows. The net radial velocity must be zero to respect mass conservation, but the distribution can be skewed. The Probability Distribution Function (PDF) of the radial velocity at r = 1.8 is shown in Figure 7. The distribution is skewed for both cases from Series 1 and 2 with a long tail in the positive values. The skewness is very evident for Series 1, with a prominent shoulder corresponding an accumulation of weak negative values. We calculate the skewness of the distribution as

$$\gamma(r) = \frac{\langle u_r^3 \rangle_{\mathcal{S}(r)}}{\langle u_r^2 \rangle_{\mathcal{S}(r)}^{3/2}},$$

where the angular brackets correspond to an average over the spherical surface S(r). Figure 7(c) shows the radial profile of $\gamma(r)$ for these two cases. Note that a limited number of data snapshots were available for the case of Series 2, so the profile shows significant fluctuations at large radii. In either case, the radial velocity is positively skewed for most of the domain and the skewness increases with radius. As expected from the PDFs, the skewness is more pronounced for wide fingers (Series 1). At radius greater than r > 2.3, where the flow is weak, the skewness drops and becomes negative in the outer boundary layer.

3.2.2. Finger clusters and toroidal gyres

In some cases with $N^2/\Omega^2 > 1$, the dynamics change in the upper half of the domain $(r \gtrsim 2)$ with the localisation of radial fingers into large-scale patches (or clusters) at high latitudes. This is illustrated in Figure 8 showing the spherical projection of u_r and u_θ at r = 2.1 for $N^2/\Omega^2 = 12.4$ in Series 2. Fingering convection in the lower half of the domain is more vigorous and there is no evidence of clustering, similarly to the dynamics observed in Figure 6(b). The patches in the upper domain are much larger scale than the transverse finger size and are accompanied by toroidal gyres. Figure 9 shows the poloidal and toroidal kinetic energy spectra as a function of the azimuthal order m at different radii for the case of Figure 8. In the lower domain, the poloidal and toroidal flows involve a wide range of azimuthal wavenumbers from m = 1 to $m \approx 50$, whilst in the upper domain, the flow is dominated by smaller azimuthal wavenumbers ($m \lesssim 20$) and is prominently toroidal. The zonal flow (toroidal m = 0 mode) dominates at all radii and will be discussed separately in section 3.5.

The clusters are associated with the presence of large-scale density anomalies that emerge in the upper domain. The fingers tend to cluster in the heavier anomalies, and are nearly absent in the lighter anomalies. Large-scale upwelling and downwelling flows are associated with these density anomalies, but they are very weak compared with the fingers in the lower domain as indicated by the spectra of Figure 9; they are also not visible in the radial profiles of the r.m.s. velocity in figure 4 for $N^2/\Omega^2 > 1$. The large-scale anomalies are more evident in the composition perturbation, so we use the composition to understand the spatial relation between anomalies and toroidal gyres. Large-scale temperature perturbations also exist, which counteract the composition perturbations; however, their amplitude is smaller,

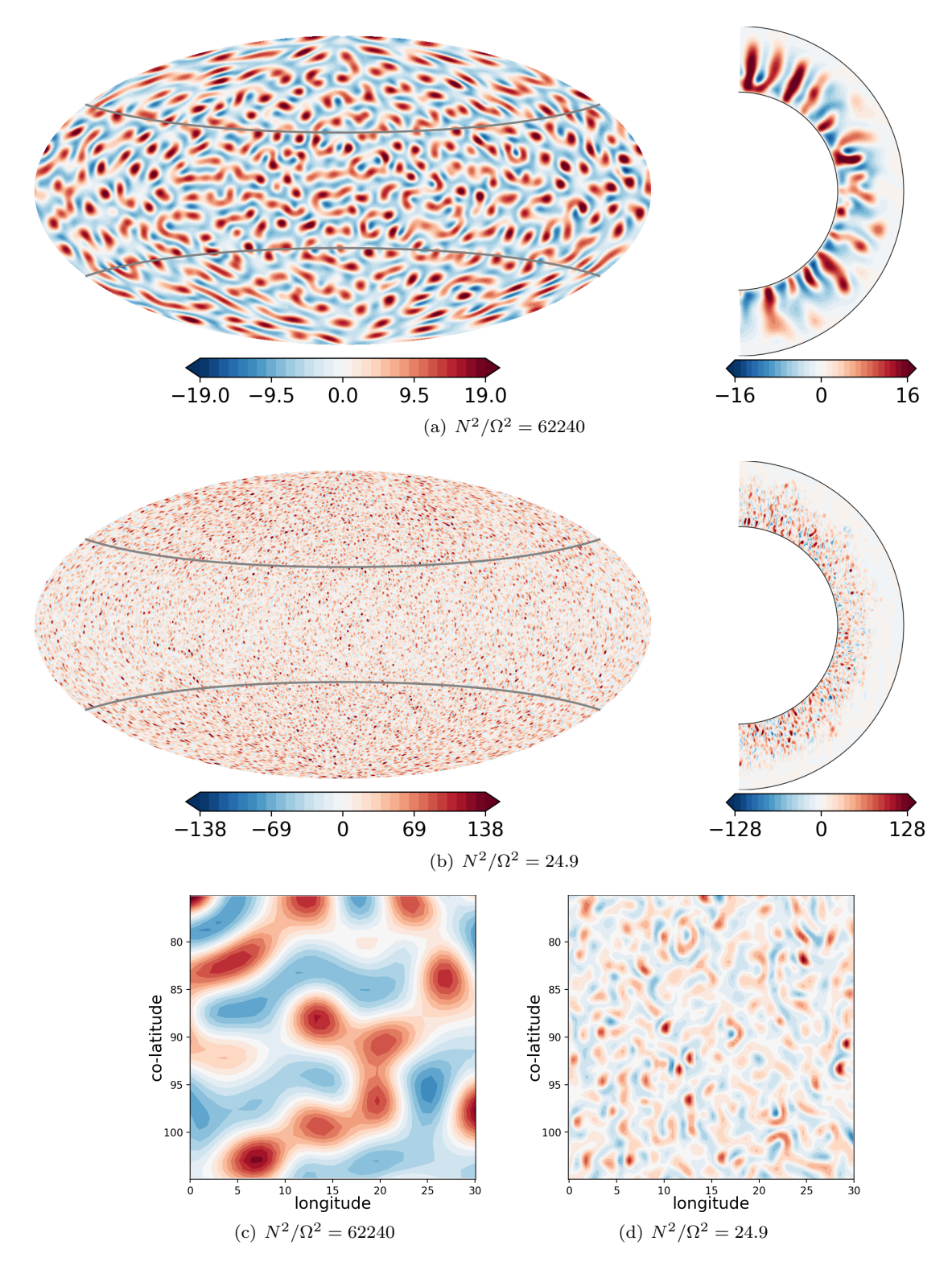


Figure 6: Snapshots of the radial velocity for simulations in the weakly-rotating regime: (a)-(b) Aitoff projection at r=1.8 (left) and meridional slice (right) for (a) $N^2/\Omega^2=62240$ in Series 1 ($Ek=10^{-1}$, $Ra_c=2\times10^7$) and (b) $N^2/\Omega^2=25$ in Series 2 ($Ek=10^{-4}$, $Ra_c=8\times10^9$). Plots (c) and (d) are close-ups of the spherical projections. In the Aitoff projections, the gray lines indicates the location of the tangent cylinder.

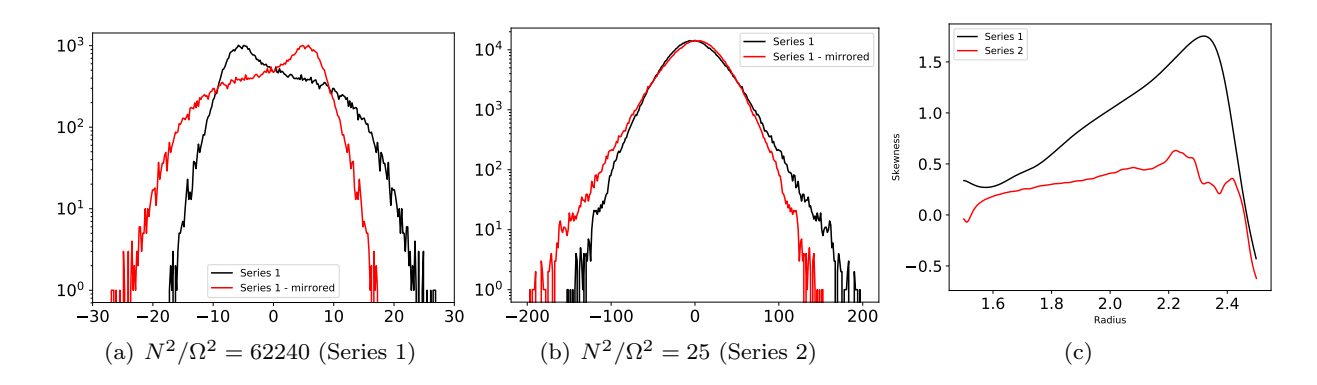


Figure 7: (a) and (b) PDF of the radial velocity at r=1.8 for $N^2/\Omega^2>1$. The distribution is mirrored with respect to x=0 to highlight the asymmetry between positive and negative values. (c) Radial profile of the skewness $\gamma(r)$ of the radial velocity.

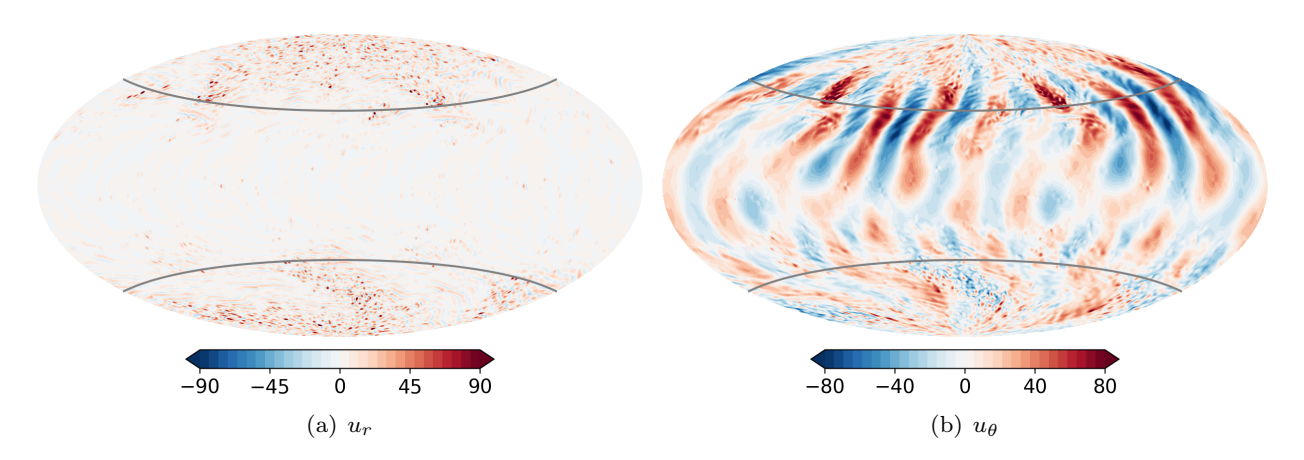


Figure 8: Aitoff projection at r = 2.1 of a snapshot of the radial and latitudinal velocities for $N^2/\Omega^2 = 12.4$ in Series 2.

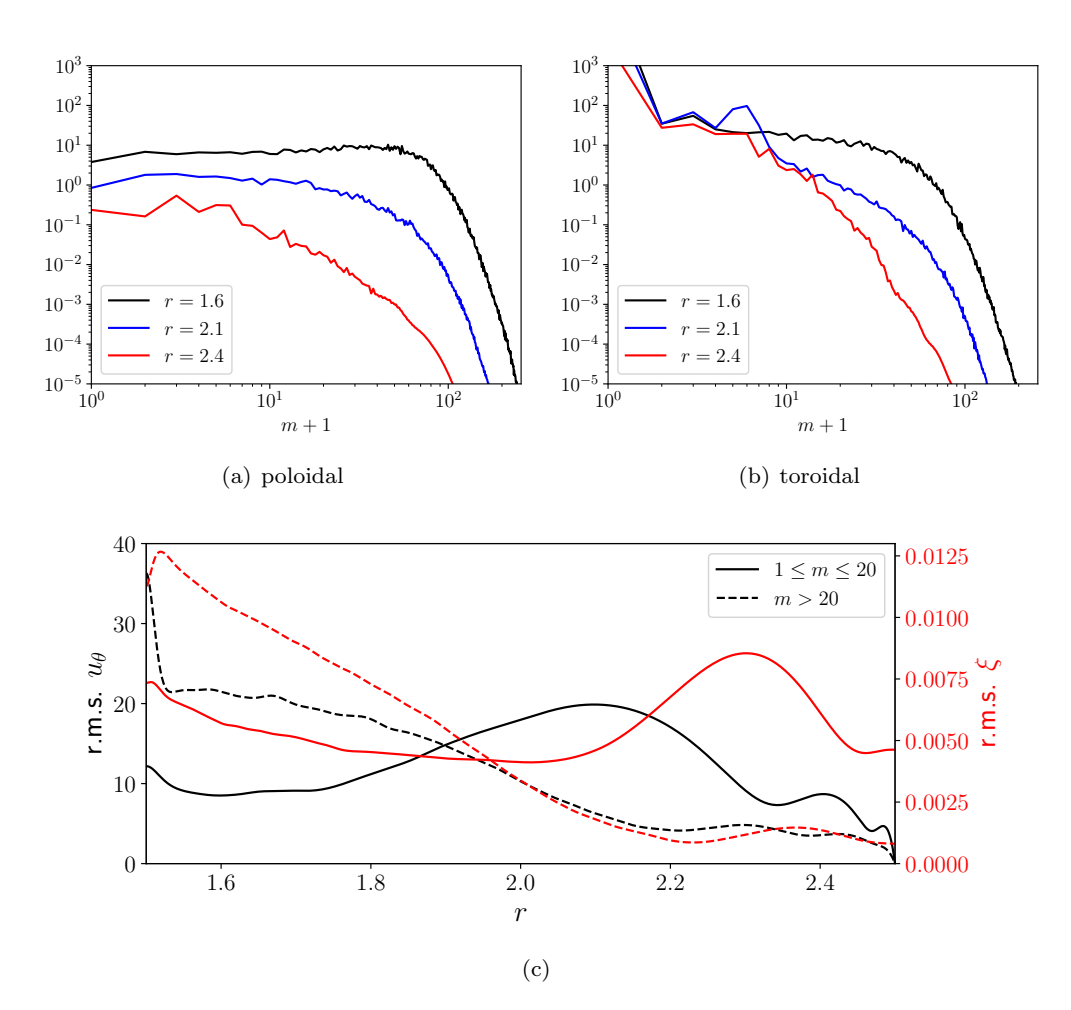


Figure 9: (a)-(b) Spectra of the poloidal and toroidal kinetic energy as a function of the azimuthal order m at different radii for $N^2/\Omega^2 = 12.4$ in Series 2. (c) Radial profiles of the filtered r.m.s. latitudinal velocity and composition perturbation. The composition perturbation is normalised by C_s at $r = r_i$.

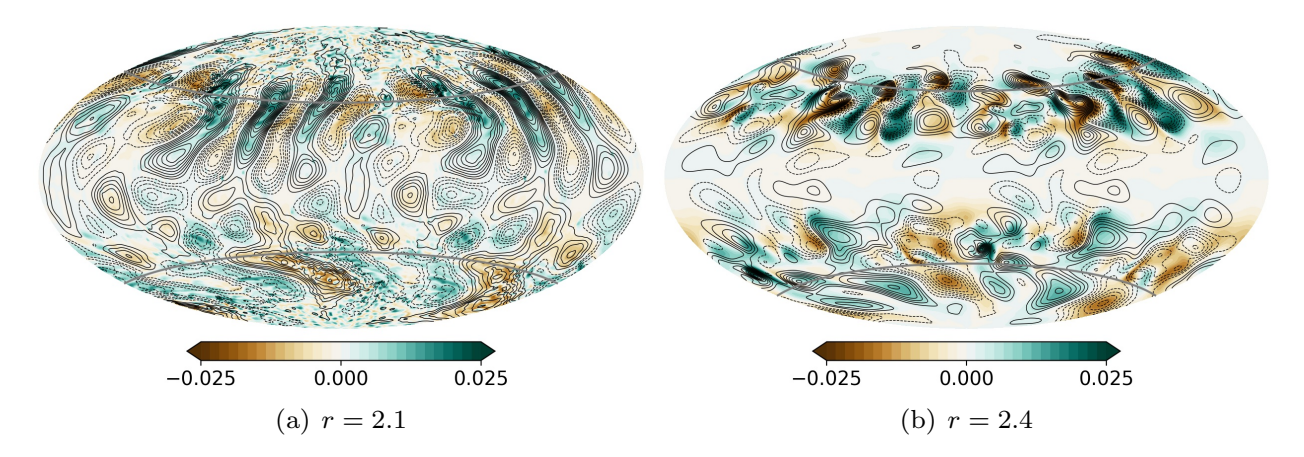


Figure 10: Isocontours of non-axisymmetric ξ (colour) and U_t (black lines) in an Aitoff projection at r=2.1 and r=2.4 for $N^2/\Omega^2=12.4$ in Series 2. The composition is normalised by C_s at $r=r_i$. For U_t , the solid (dashed) lines indicates positive (negative) contours. Anti-clockwise gyres have positive U_t .

resulting in the composition perturbations dominating the density anomalies. Figure 9(c) shows the radial profiles of the r.m.s. u_{θ} and ξ separated into large azimuthal scales ($1 \le m \le 20$) and smaller scales (m > 20). The large-scale latitudinal velocity dominates in the upper domain and the r.m.s. profile has two local peaks (located at $r \approx 2.1$ and $r \approx 2.4$) that surround a peak of the large-scale composition perturbation.

Since the flow is dominated by the toroidal component at large radii, we plot in Figure 10 isocontours of the non-axisymmetric toroidal scalar U_t and composition perturbation at radius r=2.1 and r=2.4. The location of the toroidal gyres and composition patches is clearly correlated. At r=2.1, anti-clockwise gyres ($U_t>0$) are associated with lighter patches ($\xi>0$) in the northern hemisphere, and vice-versa in the southern hemisphere. This hemispherical dependence indicates the importance of the Coriolis force in the formation of these toroidal flows. The composition patches extend through the upper domain and keep their coherence. The toroidal gyres change sign of rotation at r=2.4, i.e. clockwise gyres ($U_t<0$) are now associated with lighter patches. These observations suggest that the slow, large-scale upflows of lighter fluid draw convergent horizontal flows at the lower roots around $r\approx2.1$ and divergent horizontal flows at their top ($r\approx2.4$) (poloidal u_θ and u_ϕ not shown here); and vice-versa for downflows of heavier fluid. These convergent/divergent flows are deflected by the Coriolis force into anti-clockwise/clockwise toroidal gyres in the northern hemisphere (and vice-versa in the southern hemisphere).

The finger clusters occur in a limited range of the parameter space indicated by open circles in Figure 1. They are not visible in Series 1, which suggests that sufficiently low Ekman number might be required. To test their sensitivity to changes in N^2/Ω^2 , we ran a number of simulations at intermediate values of Ra_c indicated in Figure 1. The clusters are present for $N^2/\Omega^2 \approx 100$, but disappear for $N^2/\Omega^2 \approx 1000$, suggesting that they occur in the limited range $N^2/\Omega^2 \approx 1-100$ for $Ek \lesssim 6 \times 10^{-4}$.

Finger clustering was previously observed in Cartesian box simulations at high Pr and low density ratio (Paparella and Von Hardenberg, 2012), but this is likely through a different mechanism than observed here. Indeed, in these box simulations the clustering is defined as the formation of large-scale buoyant structures and is thought to occur via entrainment as the local Reynolds number might exceed unity. Unlike in our simulations, this occurs in the absence of rotation. Here the clustering corresponds to a spatial localisation of fingering convection. It is linked to the development of large-scale density anomalies: within the heavier anomalies, the local compositional Rayleigh number, estimated from the local radial compositional gradient, is up to four greater than in the lighter anomalies. Consequently, fingering convection is preferentially promoted in the heavier anomalies. However, we currently have no explanation for the origin of the large-scale density anomalies in the upper domain.

3.3. Rapid rotation

3.3.1. Columnar fingers

Flows in the rapid-rotation regime were described in Guervilly (2022) in the same configuration and using a larger dataset including lower Ekman numbers ($Ek \in [10^{-6}, 10^{-4}]$). The main features are summarised in this short

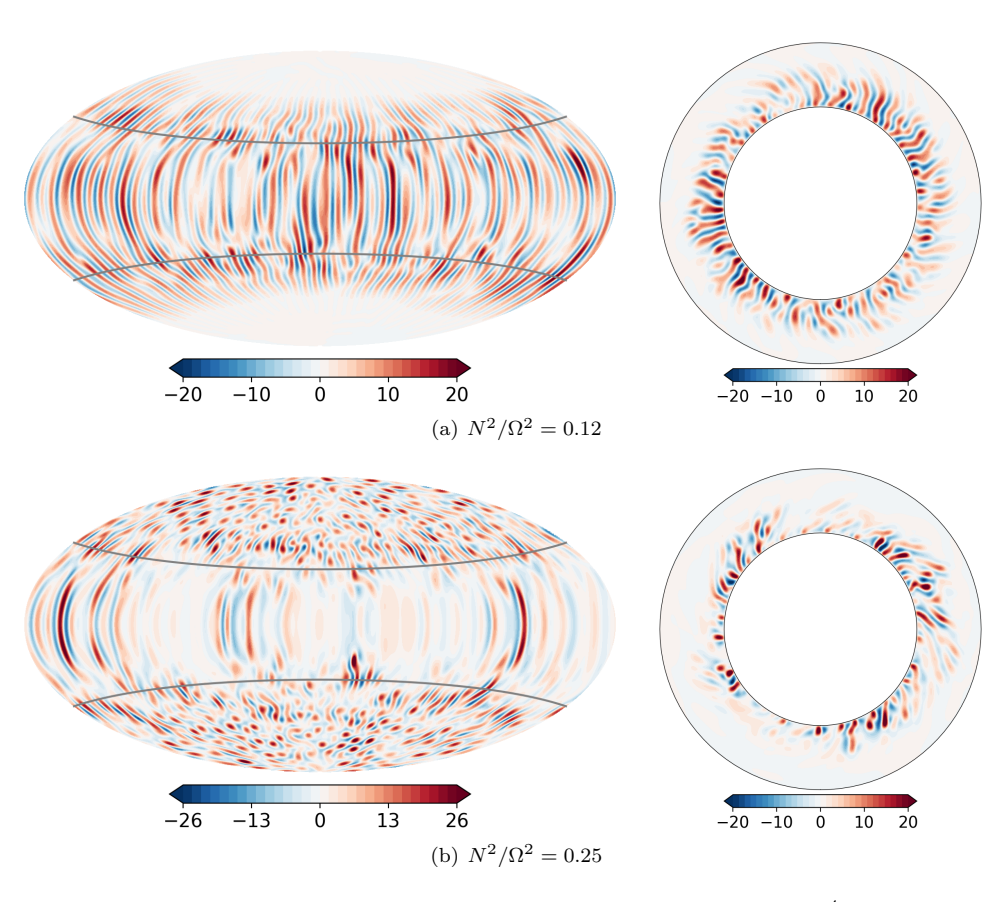


Figure 11: Snapshot of the radial velocity for simulations in the rapidly-rotating regime in Series 2 ($Ek = 10^{-4}$): Aitoff projection at r = 1.8 (left) and equatorial slice (right).

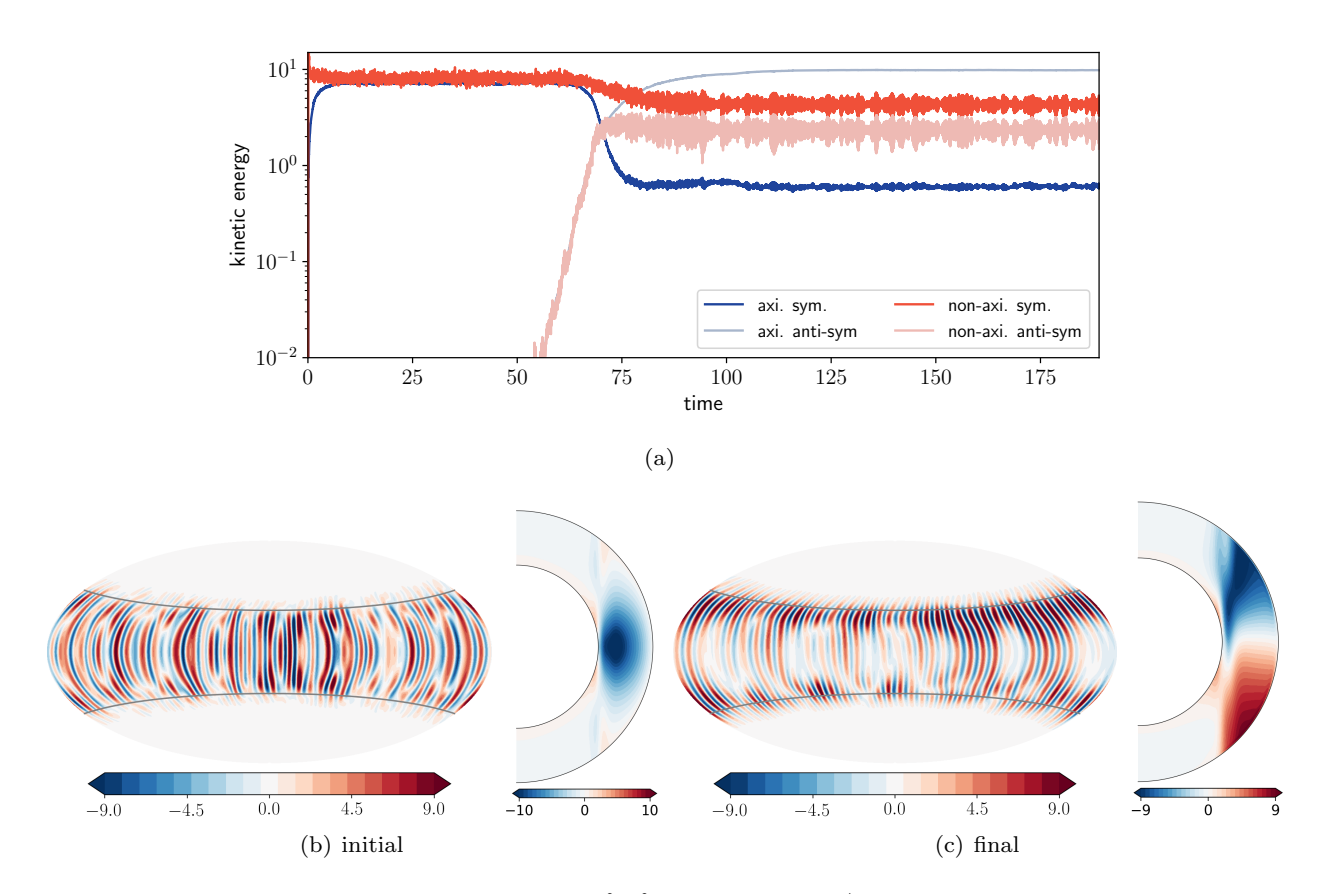


Figure 12: (a) Time series of the volumetric kinetic energy for $N^2/\Omega^2 = 0.06$ and $Ek = 10^{-4}$. Sym/anti-sym refers to the equatorial symmetry. (b)-(c) snapshots of the radial velocity at r = 1.8 and meridional slice of the zonal velocity in the initial steady state, shortly after the beginning of the simulation and in the final state.

subsection for completeness.

Figure 11 shows spherical projections and equatorial slices of the radial velocity for two cases of Series 2 with $N^2/\Omega^2 < 1$. For the smallest stratification, columnar fingers occur mainly outside of the tangent cylinder, impinging slightly inside the tangent cylinder. Larger N^2/Ω^2 leads to the development of columnar fingers in the polar regions. The radial flows gradually become stronger in the polar regions than in the equatorial regions as N^2/Ω^2 increases, whilst fingering convection become localised in the equatorial region. Zonal flows develop in the equatorial region (see section §3.5), leading to a visible shear and disruption of fingering convection in that region, which might explain why radial flows are relatively more vigorous in the polar regions.

3.3.2. Equatorially antisymmetric mode

We observe an interesting behaviour (not reported in Guervilly (2022)) from an extended running time for the simulation with $N^2/\Omega^2 = 0.06$ (which is shared by Series 1 and 2) as shown in the time series of Figure 12. The flow is columnar and located outside the tangent cylinder. In the initial steady state (Figure 12(b)), the flow is symmetric with respect to the equatorial plane (equatorially symmetric – ES) with a dominant non-axisymmetric component. Then, after over 60 viscous timescales, the flow gradually transitions to a different steady state. The transition corresponds to a change in the equatorial symmetry of the flow. After the transition (Figure 12(c)), the zonal velocity dominates and is now largely equatorially antisymmetric (EAS). Whilst the non-axisymmetric flow remains mainly ES after the transition, its amplitude is divided by a factor two (so is then only a factor of two larger than the non-axisymmetric EAS component). Note that in all the plots showing global averages (Re, Re_0 and Nu_c below), we use the values averaged before the transition for simplicity. The output quantities calculated after the transition to the EAS mode are given in Table A.2.

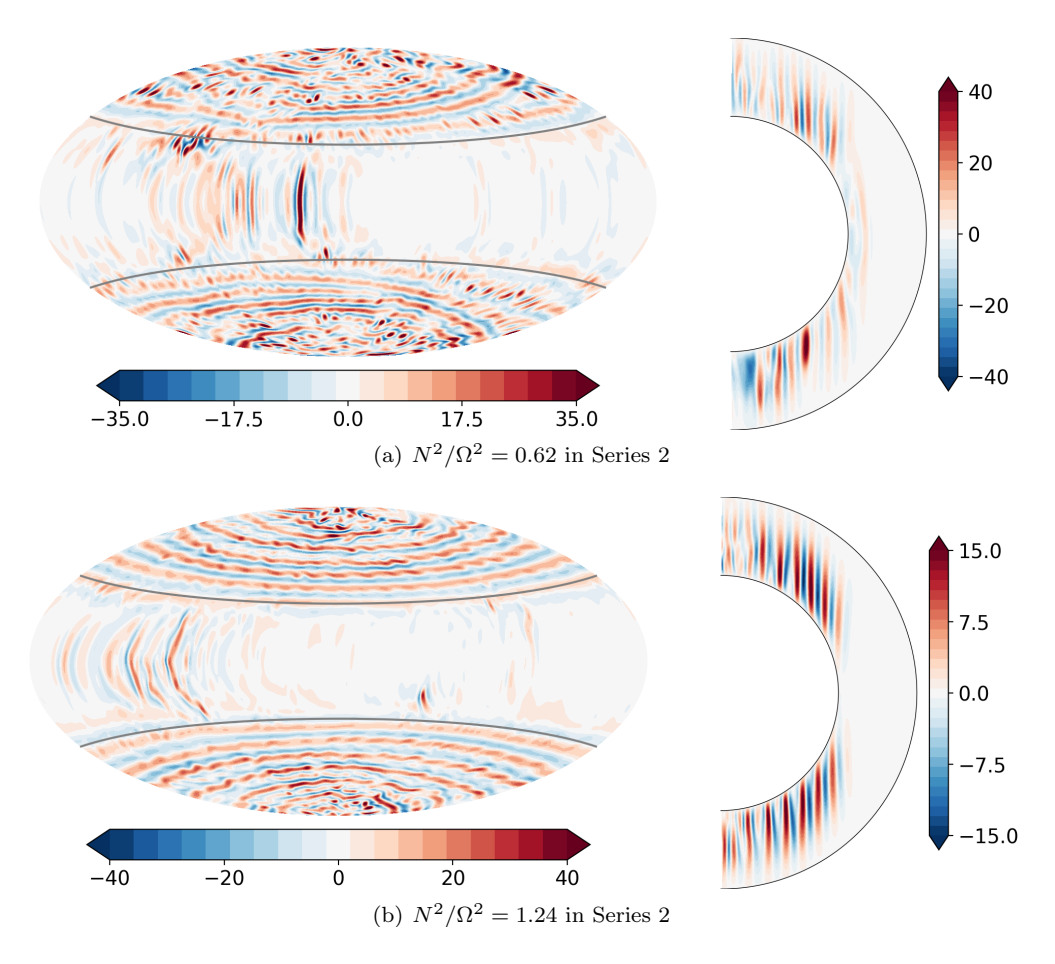


Figure 13: Snapshots of the radial velocity for simulations in the intermediate regime: (left) Aitoff projections at r = 1.8; (right) meridional slice at a given longitude. For (b), the meridional slice shows the axisymmetric component.

The transition to the EAS mode was previously observed in the simulations of fingering convection in a full sphere geometry of Monville et al. (2019). Monville et al. reported that this transition occurs for Rayleigh numbers above the linear onset for the EAS axisymmetric mode, which suggests that this mode grows linearly. This mode corresponds to hemispherical convection with EAS axisymmetric composition and temperature perturbations, where the northern hemisphere is enriched in light elements and colder than the southern hemisphere. This is the only instance where the EAS axisymmetric mode becomes dominant in our simulations, even after running simulations for multiple tens of viscous timescales. For smaller stratification, the mode decays; for larger stratification, the mode saturates at a smaller amplitude than the ES axisymmetric mode. This simulation shows that the EAS axisymmetric mode can occur in spherical shells, even for relatively large aspect ratio (here $r_i/r_o = 0.6$). As argued in Monville et al. (2019), simulations spanning many viscous times are required to observe this transition.

3.4. Intermediate regime

3.4.1. Banded structures

We now explore the intermediate regime where $N^2/\Omega^2 \approx 1$. Over timescales of the order of a viscous timescale, we observe the formation and saturation of bands of poloidal flows as shown in the spherical projection of u_r in Figure 13. These bands are persistent and only form inside the tangent cylinder. While in some cases the bands are spiraling (corresponding predominantly to an azimuthal order m=1, Figure 13(a)), in other cases the bands are predominantly axisymmetric (corresponding to m=0, Figure 13(b)). The bands have a narrow latitudinal extent compared with their azimuthal extent. The meridional slices of Figure 13 show the axial extent of the bands. The

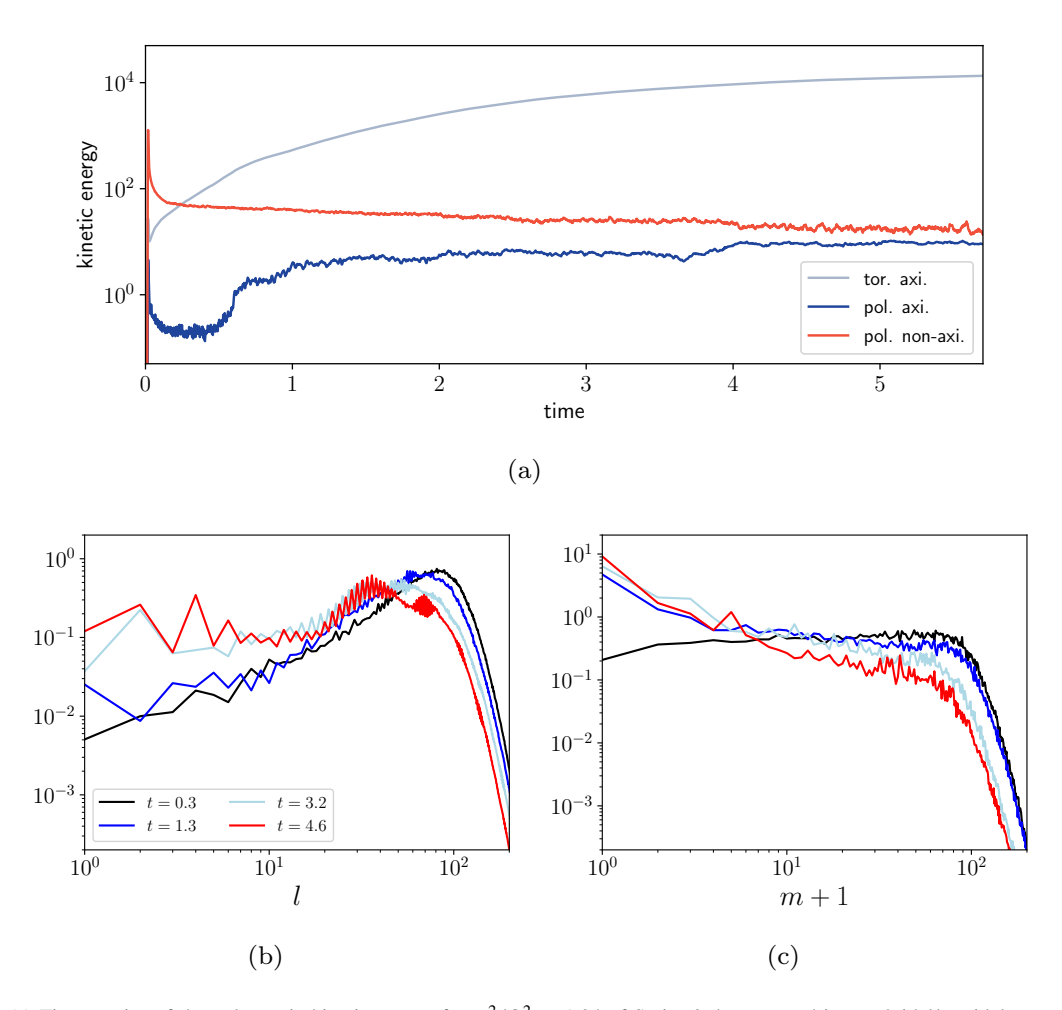


Figure 14: (a) Times series of the volumetric kinetic energy for $N^2/\Omega^2 = 1.24$ of Series 2 decomposed into poloidal/toroidal components and axisymmetric/non-axisymmetric components. (b)-(c) Spectra of the poloidal kinetic energy as a function of the spherical harmonics degree l and order m at different times of the simulation. The spectra are averaged in radius excluding the boundary layers.

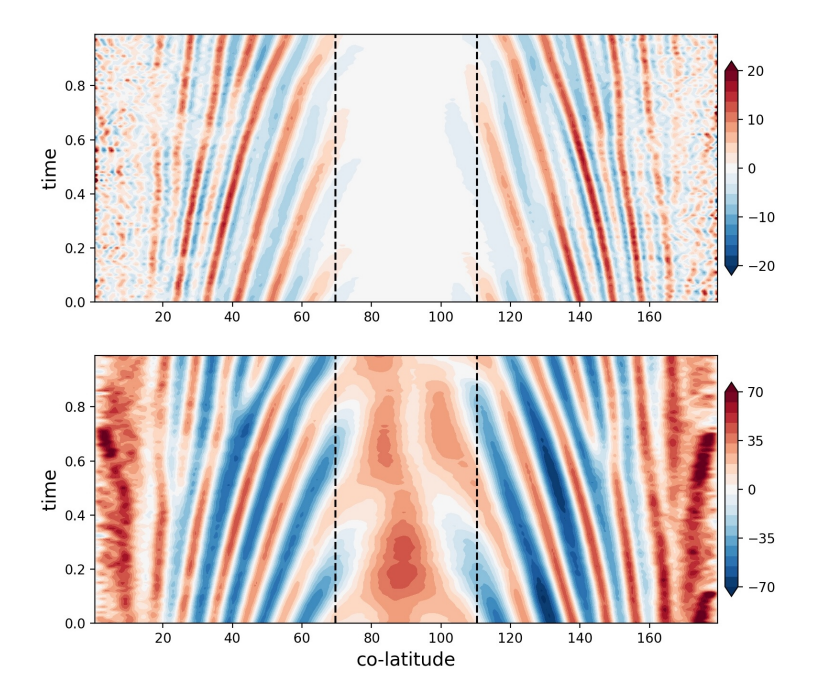


Figure 15: Space-time diagram of the axisymmetric radial (top) and azimuthal (bottom) velocities at r = 1.6 for $N^2/\Omega^2 = 1.24$ of Series 2. The spherical harmonics degree l = 1 has been removed from the azimuthal component to filter out the dominant equatorial prograde zonal flow. The dashed line corresponds to the intersection with the tangent cylinder for this radius.

bands are essentially concentric cylindrical structures aligned with the rotation axis. The radial flows in the equatorial regions are comparatively weak, which might be due to the presence of strong zonal flows that can disrupt convection in this region. Indeed, the amplitude of the zonal flow is maximal in the intermediate regime, exceeding the amplitude of the radial flows by one order of magnitude (see section §3.5).

Figure 14 shows the times series of the kinetic energy and the power spectra of the poloidal kinetic energy at different times of the simulation at $N^2/\Omega^2=1.24$ of Series 2. The fingers initially develop at a size close to the Stern scale (around $l\approx m\approx 80$), but the energy then builds up at small m, with a dominant m=0, and around about $l\approx 40$. Meanwhile the energy at the Stern scale gradually decreases before reaching saturation at a lower energy level than the bands. The fingers might be losing energy to the benefit of the bands, either due to a decrease of the mean composition gradient in the bulk or due to non-linear energy transfers, or because of the progressive increase of the zonal flow, which finally reaches saturation after t>5. At saturation (t=4.6), the bands carry a similar amount of kinetic energy to the initial fingers at the Stern scale (at t=0.3). Their associated local Reynolds number is thus greater (as their latitudinal scale are larger), but remains below unity.

To study the temporal behaviour of the bands in the saturated regime, Figure 15 shows a space-time diagram of the axisymmetric radial velocity at a fixed radius close to the inner boundary (r = 1.6). The time period corresponds to approximately one viscous timescale (one unit of dimensionless time). For latitudes smaller than $\pm 70^{\circ}$, the bands slowly drift latitudinally over time towards the equatorial region, eventually disappearing on the tangent cylinder. New drifting bands nucleates over time around latitudes of $\pm 70^{\circ}$. At higher latitudes, weak meandering bands can be seen and appear to be drifting towards the poles.

Azimuthal velocities are associated with the presence of the bands of poloidal flows. Similarly, they show a spiraling or axisymmetric pattern. They can be seen inside the tangent cylinder in Figure 17(c) in §3.5 with a smaller amplitude than the equatorial prograde zonal. To observe their temporal evolution, we filter out the spherical harmonics degree l = 1 in the post-processed data, which is the main component of the equatorial zonal flow. The space-time diagram of the filtered axisymmetric azimuthal velocity is shown in Figure 15 and reveals that the latitudinal drift is also seen in the banded azimuthal flow.

The bands have a narrow range of existence, only appearing for parameters around $N^2/\Omega^2 \approx 1$ (see Figure 1).

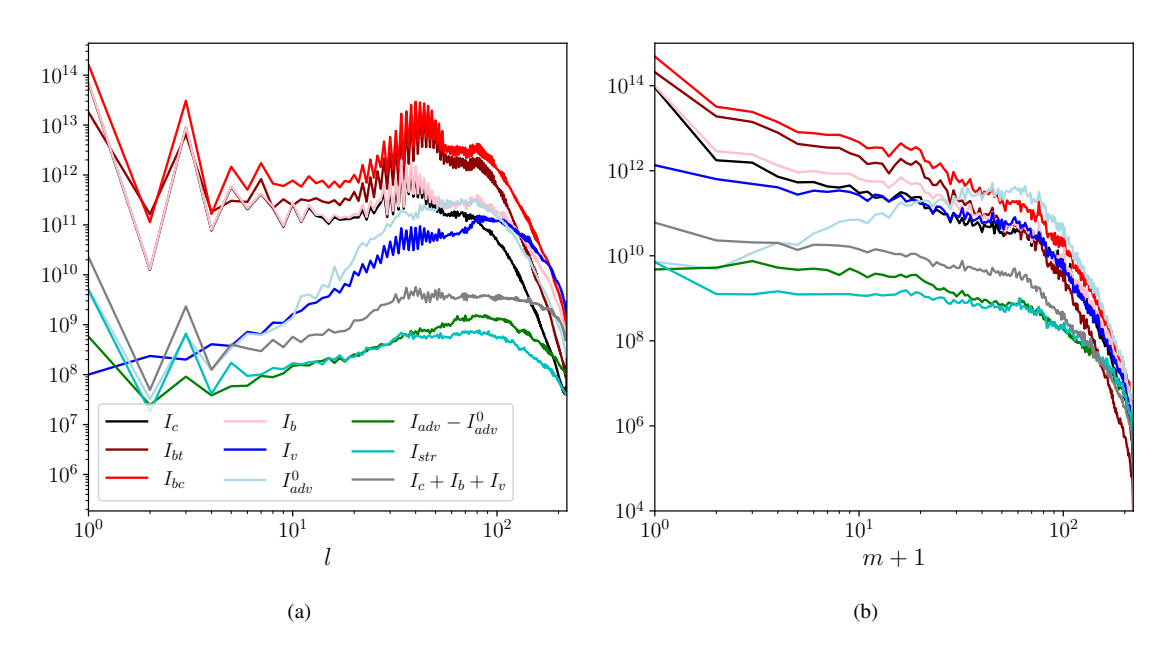


Figure 16: Spectral representation of each terms in the equation for ϕ -component of the vorticity (equation (24)) for the case $N^2/\Omega^2 = 1.24$ of Series 2. The spectra are averaged in radius between 1.6 and 2. I_c corresponds to the Coriolis term; I_{bt} and I_{bc} to the thermal and compositional buoyancy terms; I_v to the viscous term; I_{adv}^0 and $I_{adv} - I_{adv}^0$ to the advection by the zonal and non-zonal velocity; I_{str} to vortex stretching. The total buoyancy $I_b = I_{bt} + I_{bc}$ and the residual $I_c + I_b + I_v$ are calculated in the physical space before calculating the spectral decomposition.

Varying the buoyancy frequency by more than one order of magnitude above or below this threshold value leads to a transition to radial or columnar fingers respectively. The bands are robust features in the sense that they occur for $N^2/\Omega^2 \approx 1$ irrespective of Ek or Ra_c (i.e. they appear in both Series 1 and 2 and in additional simulations shown in Figure 1), at least for the density ratio used here.

3.4.2. Origin of the bands

We conclude this section by studying the origin of the bands. In particular, we want to understand the role of the non-linear interactions in the formation of the bands. First, we compare the relative importance of the forces in the Navier-Stokes equation at different scales. This is most easily done by comparing the sources of the vorticity $\omega = \nabla \times \mathbf{u}$. Since the bands correspond essentially to axisymmetric or m = 1 poloidal flows, we analyse the relative strengths of the terms in the equation for the ϕ -component of the vorticity:

$$\frac{\partial \omega_{\phi}}{\partial t} + \left[(\mathbf{u} \cdot \nabla) \omega \right]_{\phi} - \left[(\omega \cdot \nabla) \mathbf{u} \right]_{\phi} - \frac{2}{Ek} \frac{\partial u_{\phi}}{\partial z} = \left[\nabla^{2} \omega \right]_{\phi} - \frac{1}{r_{o}} \left(\frac{\partial \Theta}{\partial \theta} + \frac{\partial \xi}{\partial \theta} \right). \tag{24}$$

For a given snapshot, we calculate the power spectra of each term as a function of the spherical harmonics degree l or order m. The goal here is to determine whether the force balance differs for the bands and the fingers. Figure 16 shows the power spectra for the case of Figure 14. The spectra are averaged in radius between 1.6 and 2, where the bands have the strongest amplitude, and calculated at a time where the system is in a statistically steady-state. For spherical harmonics degrees and orders smaller than $l \leq 100$ and $m \leq 30$, the dominant vorticity sources are the thermal and compositional buoyancy terms (last term on the right-hand side (RHS) of equation (24)). They partially cancel each other as shown by the lower value of the total buoyancy for these scales. The thermal diffusion wipes out smaller scales and the thermal buoyancy drops out more rapidly than the compositional buoyancy in the spectral tail. At the scale of the bands (m = 0, 1 and $l \approx 40$), the main balance for the generation of the azimuthal vorticity is between the buoyancy term and the Coriolis term (last term on the left-hand side (LHS) of (24)). At the finger scale ($l \approx 80$), the viscous term (first term on the RHS) also enters this balance. The non-linear inertial terms (2nd and 3rd terms in the LHS) are significantly smaller than buoyancy, viscous and Coriolis terms at all scales, except for

the advection by the zonal velocity which is dominant at the finger scale. Using snapshots at earlier times during the growth of the bands gives the same picture, suggesting again that inertia is unimportant for the formation of the bands.

To confirm this, we performed a linear simulation for $N^2/\Omega^2 = 1.24$ of Series 2, where all the non-linear terms are switched off in XSHELLS: the mode m = 0 grows and forms banded structures inside the tangent cylinder similar to those described in the non-linear calculations. We therefore conclude that the bands corresponds to a linear mode of fingering convection, which is preferred when $N^2/\Omega^2 \approx 1$ for this density ratio.

3.5. Zonal Flow

3.5.1. Formation of the zonal flow

Fingering convection produces persistent zonal flows in the presence of rotation. They are equatorially symmetric (except for the case $N^2/\Omega^2=0.06$ reported in §3.3.2) and their speed can exceed the amplitude of the radial velocities. Guervilly (2022) showed that the zonal flow is produced by a linear process and is in a thermo-compositional wind balance, where the latitudinal variations of the axisymmetric density perturbations are balanced by axial variations of the zonal velocity. The thermo-compositional wind balance is derived from the equation for ω_{ϕ} (equation (24)) in an axisymmetric, steady state and neglecting the non-linear and viscous terms,

$$\frac{2}{Ek}\frac{\partial \overline{u_{\phi}}}{\partial z} \approx \frac{1}{r_o} \left(\frac{\partial \overline{\Theta}}{\partial \theta} + \frac{\partial \overline{\xi}}{\partial \theta} \right), \tag{25}$$

where the overline denotes an azimuthal average. For rapidly-rotating fingering convection, the latitudinal difference in the mixing of composition and temperature is a source of baroclinicity, driving a meridional circulation that is deflected into *z*-dependent zonal flows by the Coriolis force. Composition and temperature gradients oppose each other, but the slower diffusion of the composition leads to sharper composition gradients, which dictate the direction of the meridional circulation and zonal flows.

Figure 17 shows meridional slices of the zonal velocity and the axisymmetric composition perturbation for increasing N^2/Ω^2 . For the smallest N^2/Ω^2 , the zonal flow is retrograde in the equatorial region and is associated with a compositional mixing that solely takes place outside the tangent cylinder, as the polar regions are not convecting (Figure 11(a)). As fingering convection onsets in the polar regions at larger N^2/Ω^2 (Figure 11(b)), the mixing becomes more efficient at high than low latitudes and the latitudinal compositional gradient is reversed. This leads to a reversal in the direction of the zonal flow, which is strongest outside the tangent cylinder. Further increase of N^2/Ω^2 up to approximately 10 leads to an amplification of the latitudinal dependence in the mixing and an intensification of the prograde zonal flow. As N^2/Ω^2 is increased further in the weak-rotation regime, the mixing becomes increasingly homogeneous with latitude, leading a gradual weakening of the zonal flow. At our largest stratification $(N^2/\Omega^2 = 62240)$, the zonal flow is significantly weaker than the radial flows; we expect that it would eventually completely disappear as $N^2/\Omega^2 \to \infty$.

3.5.2. Scaling of the zonal velocity

Figure 18(a) shows the variation of the Reynolds number based on the zonal flow amplitude, $Re_0 = V_0 D/\nu$, where V_0 is the mean zonal velocity calculated from the volume and time average of the axisymmetric toroidal kinetic energy. Re_0 increases until $N^2/\Omega^2 \approx 10$ for both Series, and then decreases for larger values. At its maximum, Re_0 reaches a value approximately 10-30 times larger than Re. This suggests that large values of the zonal flow can be reached at low Ekman numbers.

Around $N^2/\Omega^2 = 0.2$, a discontinuity is visible in the variation of Re_0 . This corresponds to the onset of fingering convection inside the tangent cylinder, which is accompanied by a reversal of the direction of the zonal flow, from retrograde (as in Figure 17(a)) to prograde (Figure 17(b)). The case $N^2/\Omega^2 = 0.2$ of Series 1 exhibits a transition from the initial (weaker) retrograde state to the final (stronger) prograde state after a long integration time of approximately 35 viscous timescales.

In the rapidly-rotating regime, Guervilly (2022) obtain an approximate scaling for the zonal flow amplitude by assuming a compositional wind balance, where only the latitudinal gradients of the composition balance with the axial gradient of the zonal velocity on large scales. Since the diffusion of the composition perturbations is slow compared with its advection, the scaling then assumes that the composition perturbations are of the same order of magnitude as

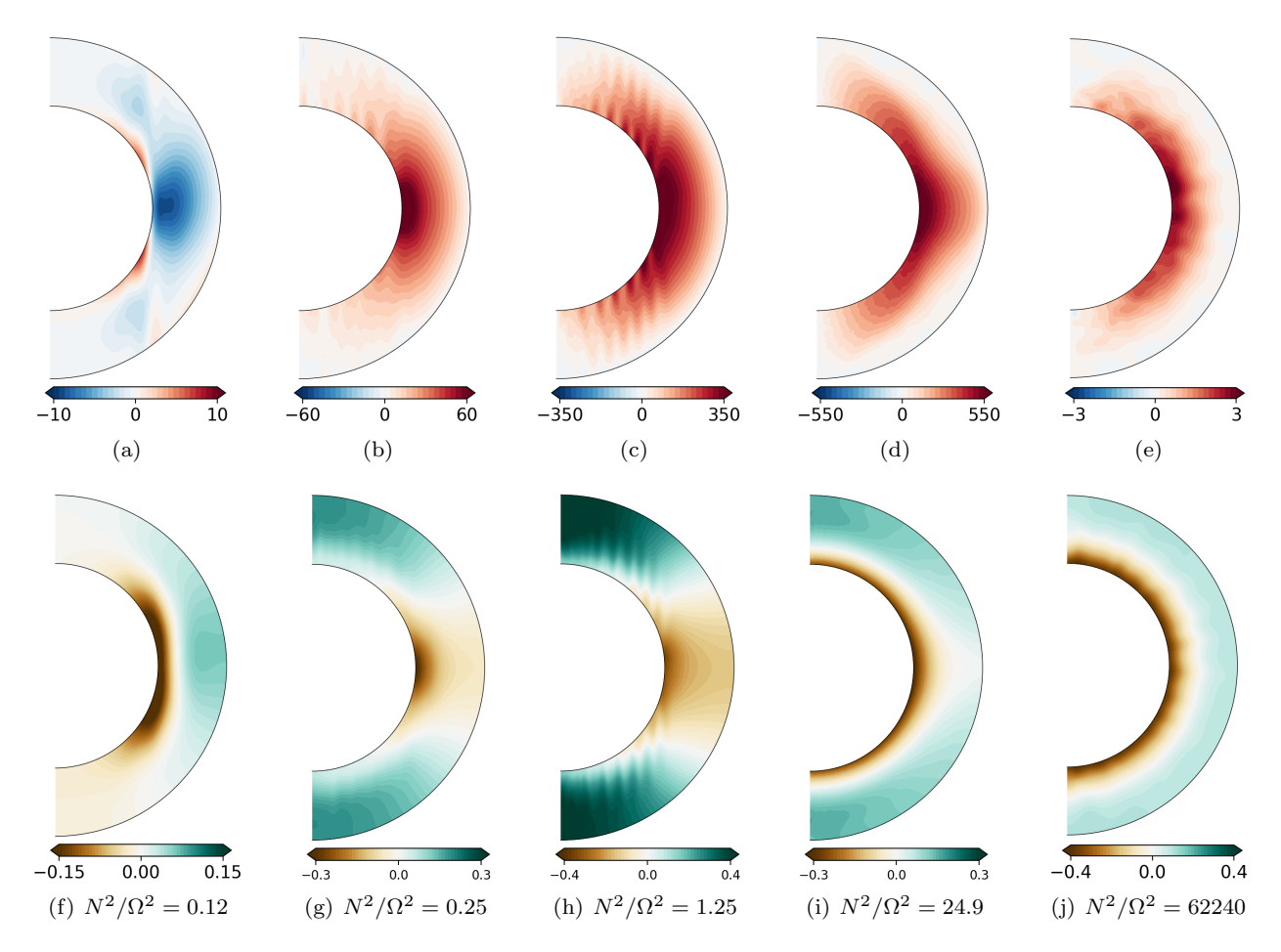


Figure 17: Meridional slices of the zonal velocity (top row) and the axisymmetric composition perturbation (bottom row) for simulations in Series $2(N^2/\Omega^2 \in [0.12, 25])$ and Series $1(N^2/\Omega^2 = 62240)$. The composition is normalised by the basic state composition C_s at $r = r_i$.

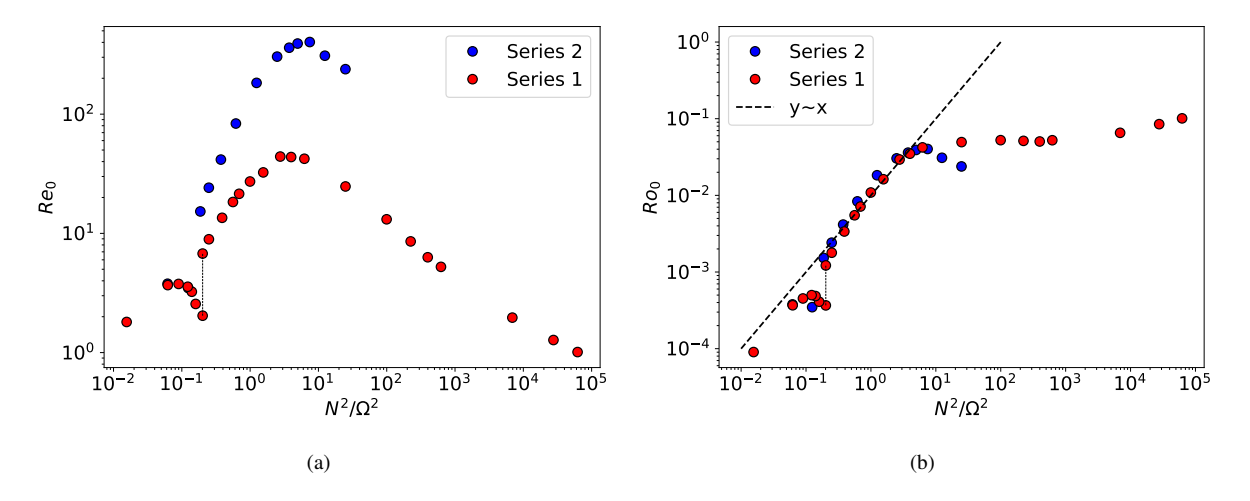


Figure 18: Variation of (a) the zonal Reynolds number and (b) the zonal Rossby number as a function of N^2/Ω^2 . The dashed line in (b) corresponds to $Ro_0 = Re_0 Ek = 10^{-2} N^2/\Omega^2$. The two solutions of the bistable case at $N^2/\Omega^2 = 0.2$ are linked by a dotted line.

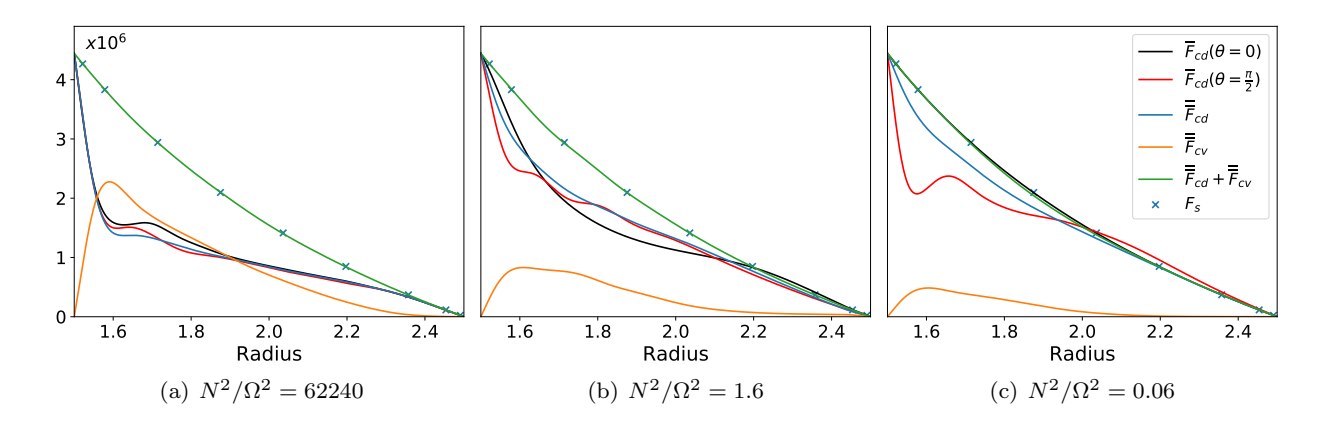


Figure 19: Radial profiles of the convective (F_{cv}) and conductive (F_{cd}) fluxes of composition for (a) the weakly-rotating, (b) the intermediate, and (c) the rapidly-rotating regimes from Series 1. The static flux in the absence of motion, F_s , is shown for comparison. Azimuthal averages are denoted by a single overbar and spherical averages by a double overbar. The fluxes have been calculated from snapshots.

the variation of the static composition over a mixing length. Assuming that the mixing length is of the order of the layer depth, the scaling becomes

$$Ro_0 = Re_0 Ek \sim \frac{1}{r_i (R_o(r_i) - 1)} \frac{N^2}{\Omega^2}.$$
 (26)

Figure 18(b) shows that the data follow reasonably well the linear dependence on N^2/Ω^2 predicted by the theoretical scaling for $N^2/\Omega^2 \lesssim 10$. We determine empirically that $Ro_0 = 10^{-2}N^2/\Omega^2$, meaning that the maximum value for Ro_0 is expected to be 0.1 (for $N^2/\Omega^2 = 10$) irrespective of the Ekman number. For $N^2/\Omega^2 \geq 100$, the Rossby number becomes a less meaningful measure of zonal flow amplitude as $Ek \to 0$ in Series 1. Simulations at higher Rayleigh numbers and constant Ekman numbers, analogous to Series 2 but currently beyond computational reach, would likely reveal a decreasing trend of Ro_0 with increasing N^2 .

3.6. Compositional transport

In this last result section, we study the mixing of the composition throughout the layer. We do not consider the convective heat transport since it is small compared with the conductive heat flux in fingering convection at low Prandtl numbers (Garaud, 2018; Guervilly, 2022; Tassin et al., 2024). We first look at the radial distribution of the convective flux, then its latitudinal dependence in the different regimes, and, finally, the global efficiency measured by a Nusselt number.

3.6.1. Radial and latitudinal dependence

The averaged convective and conductive fluxes of composition over a spherical surface $\mathcal{S}(r)$ are defined respectively as

$$\overline{\overline{F}}_{cv} = Sc \int_{S(r)} u_r \xi dS, \quad \overline{\overline{F}}_{cd} = -\int_{S(r)} \frac{\partial \xi}{\partial r} dS + F_s(r)$$
 (27)

where the double overbar denotes a spherical average and the static flux is $F_s(r) = -C'_s$.

Figure 19 shows the radial profiles of \overline{F}_{cv} and \overline{F}_{cd} for the three different dynamical regimes for selected cases in Series 1. The sum of the convective and conductive fluxes equal the static flux at all radii, as expected from a steady state. For $N^2/\Omega^2\gg 1$, the amplitude of the convective flux is comparable to the conductive flux in the lower domain of the layer where fingering convection is most vigorous. The conductive fluxes in the polar regions ($\overline{F}_{cd}(\theta=0)$), where the single overbar denotes an azimuthal average) and in the equatorial region ($\overline{F}_{cd}(\theta=\pi/2)$) are similar, thereby confirming that there is no notable latitudinal difference when the rotational effects are weak.

For $N^2/\Omega^2 \approx 1$, a reduction in convective flux is observed. In the polar regions, where the bands are present, the conductive flux slightly diminishes at mid-radius compared with other latitudes, indicating that the bands enhance compositional mixing somewhat more effectively than the sheared fingers in the equatorial region.

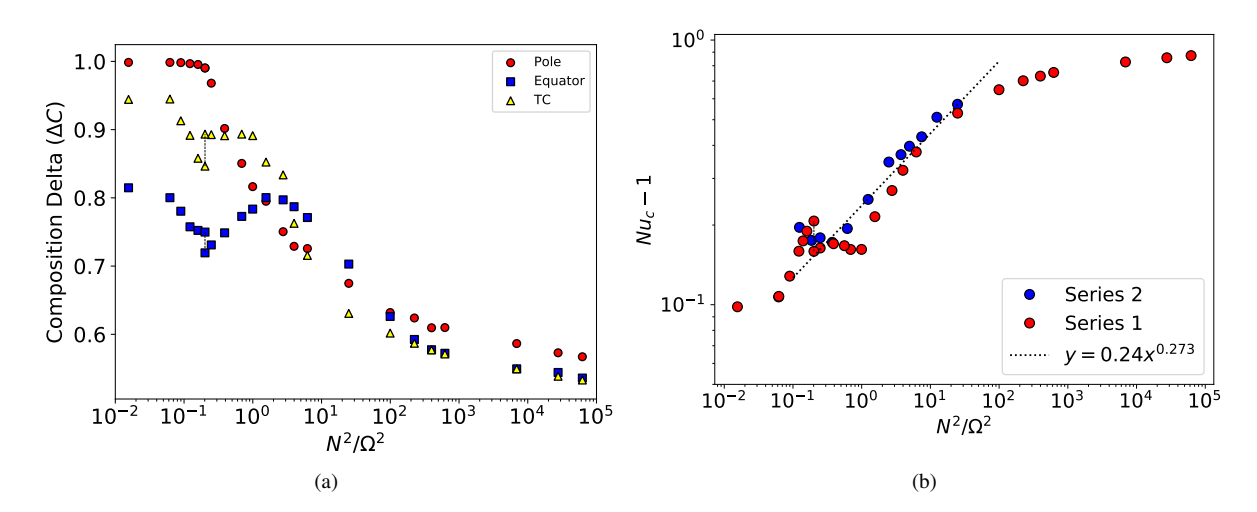


Figure 20: (a) Variation of ΔC at different latitudes as a function of N^2/Ω^2 for Series 1. (b) Variation of Nu_c-1 as a function of N^2/Ω^2 . The two solutions of the bistable case at $N^2/\Omega^2=0.2$ are linked by a dotted line.

For $N^2/\Omega^2 \ll 1$, the convective flux is further reduced and significantly smaller than the conductive flux throughout the layer. A large disparity between high and low latitudes is observed: only the region outside the tangent cylinder is convecting, so the conducting flux in the polar regions is superposed onto the static flux.

To study systematically the latitudinal dependence of the transport efficiency as a function of N^2/Ω^2 , we measure the normalised composition difference across the layer at a given latitude

$$\Delta C(\theta) = \frac{\overline{C}(r_o, \theta) - \overline{C}(r_i, \theta)}{C_s(r_o) - C_s(r_i)},\tag{28}$$

where, as previously, the overbar denotes an azimuthal average. Because fixed compositional fluxes are imposed at both the inner and outer boundaries, we expect ΔC to decrease as the mixing efficiency increases. Figure 20(a) shows the values of ΔC averaged over a $\pm 5^{\circ}$ angle around three latitudes for Series 1: the north pole ($\theta = 0$), the equator ($\theta = \pi/2$), and the latitude where the tangent cylinder intersects the outer boundary ($\theta = 0.93$ rad).

For $N^2/\Omega^2 \ll 1$, as expected, $\Delta C = 1$ at the poles since there is initially no convection inside the tangent cylinder and transport occurs only in the equatorial region. The behaviour becomes notably non-monotonic in the rapidly-rotating regime at low latitudes, with a distinct discontinuity at $N^2/\Omega^2 = 0.2$, coinciding with the onset of convection in the polar regions. This discontinuity is associated with the reversal of the zonal flow and a pronounced increase in its amplitude (Figure 18(b)), indicating an intensification of radial shear. Given the slight reduction in the poloidal Reynolds number following this transition (see Table A.1), the observed increase of ΔC at low latitudes is likely a consequence of the enhanced shear, which may act to suppress convective transport.

For weak rotation ($N^2/\Omega^2 > 100$), ΔC attains similar values across latitudes, although the poles tend to exhibit slightly smaller values. This homogenisation of mixing is consistent with the gradual disappearance of zonal flows in this regime.

In the intermediate regime $(1 \le N^2/\Omega^2 \le 10)$, ΔC at high latitudes is slightly smaller than at the equator, confirming moderately enhanced mixing associated with the bands inside the tangent cylinder.

3.6.2. Nusselt number

The efficiency of convective transport is commonly quantified by a global measure, the Nusselt number, which compares the total heat flux to the conductive heat flux at rest. In systems with fixed-flux boundary conditions, the Nusselt number can be determined from the spherically-averaged temperature difference across the layer (Mound and Davies, 2017; Monville et al., 2019). Thus, by analogy, we define the "compositional" Nusselt number (sometimes

called the Sherwood number) as

$$Nu_c = \frac{C_s(r_o) - C_s(r_i)}{\overline{\overline{C}}(r_o) - \overline{\overline{C}}(r_i)}.$$
 (29)

It is inversely related to the previously defined ΔC , but provides a global measure across the entire layer, allowing its variation with control parameters to be compared with scaling predictions from the literature.

A power-law scaling of the form $Nu_c-1=ARa_c^{1/3}$ (where the constant A depends on Pr, Le, and R_ρ) has long been proposed based on dimensional arguments (Turner, 1967). This scaling has been observed in non-rotating, plane-layer experiments and numerical simulations for Pr>1 (e.g. Radko and Stern, 2000; Hage and Tilgner, 2010). Extending the Rayleigh–Bénard convection theory of Grossmann and Lohse (2000), Yang et al. (2015) demonstrated that the 1/3 law is expected in the asymptotic regime of large Ra_c for fingering convection. In contrast, for small Pr, Brown et al. (2013) proposed an alternative scaling in which Nu_c remains constant for fixed values of Pr, Le, and R_ρ within the regime $r_\rho \ll (1/Le, Pr) \ll 1$ (noting that, although this regime is the closest for our simulations where Pr=0.3, Le=10 and $r_\rho=0.26$, it is not strictly satisfied). In the absence of rotation, Tassin et al. (2024) reported a best-fit scaling of $Nu_c-1 \sim Ra_c^{0.27}$ from numerical simulations spanning a broad range of Prandtl numbers ($Pr \in [0.03, 7]$). They attributed the deviation from the 1/3 law to the non-negligible contribution of dissipation within the boundary layers, while the 1/3 law in Grossmann and Lohse (2000) assumes bulk-dominated dissipation. In the rapidly-rotating regime with $N^2/\Omega^2 < 1$, Guervilly (2022) found that the 1/3 scaling remains a reasonable fit for constant density ratio, albeit with an additional dependence on the Ekman number.

We now examine how our simulations, which span a broad range of N^2/Ω^2 at fixed density ratio, compare with the scaling behaviours discussed above. Figure 20(b) shows the compositional Nusselt number for both Series as a function of N^2/Ω^2 . Across all cases, the convective enhancement remains modest, $Nu_c - 1 < 1$, indicating that convective fluxes are relatively weak. In the rapidly-rotating regime, the behaviour of Nu_c is non-monotonic, mirroring the behaviour of ΔC with a discontinuity at $N^2/\Omega^2 = 0.2$. The regional behaviours inside and outside the tangent cylinder act in opposition: the onset of fingering convection inside the tangent cylinder enhances convective transport, whereas the intensified shear in the equatorial region following the zonal flow reversal suppresses it. Overall, this results in a slight decrease in Nu_c at the transition.

For the range $0.2 < N^2/\Omega^2 < 1$, Nu_c remains approximately constant in Series 1, in line with the plateau observed in the poloidal Reynolds number over the same interval. In the intermediate regime, $1 \le N^2/\Omega^2 \le 10$, Nu_c begins to increase, mirroring the trend observed in Series 2. As anticipated for $N^2/\Omega^2 > 100$, Nu_c asymptotes to a plateau, indicating the transition to the $Ek \to 0$ dynamics in Series 1. To facilitate comparison with previous studies, we fit a power-law scaling of the form $Nu_c - 1 \sim (N^2/\Omega^2)^{\alpha}$ over the range $1 < N^2/\Omega^2 < 30$, despite noticeable scatter in the data. The best fit across both Series yields an exponent $\alpha \approx 0.27$, closely matching the non-rotating scaling reported by Tassin et al. (2024).

4. Conclusions

We have conducted numerical simulations of fingering convection in a thick spherical shell under the influence of rotation. Our study examined how the dynamics change as a function of the stratification strength N measured relative to the rotation rate Ω , by varying the Ekman number at fixed Rayleigh numbers (Series 1) or by varying the Rayleigh numbers at fixed Ekman number (Series 2). Throughout, the density ratio was fixed at $R_{\rho}^{i} = 3.33$ at the inner radius, as were the diffusivity ratios (Pr = 0.3 and Le = 10). We found that the dynamics depend strongly on the parameter N^{2}/Ω^{2} , with three distinct regimes emerging: a weakly-rotating regime for $N^{2}/\Omega^{2} > 10$, a rapidly-rotating regime for $N^{2}/\Omega^{2} < 1$, and an intermediate regime for $1 < N^{2}/\Omega^{2} < 10$.

In all regimes, the primary fingering mode forms narrow, elongated fingers that align with the rotation axis when $N^2/\Omega^2 < 10$, and with gravity when $N^2/\Omega^2 > 10$. The fingers remain laminar, with local Reynolds numbers below unity. Their transverse scale \mathcal{L} approximately follows the Stern scale $\mathcal{L}_{theo} = (|Ra_t|/r_o)^{-1/4}$ and, for our fixed density ratio, is well described by $\mathcal{L} = 5\mathcal{L}_{theo}$, independent of the Ekman number. For Mercury's core with a stable layer of thickness 800 km, the predicted transverse finger scales is approximately 50 - 0.5 m for $N^2/\Omega^2 = 10^{-4} - 10^4$ for the moderate density ratio considered here. In non-rotating fingering convection simulations, Tassin et al. (2024) found that the finger size depends only weakly on the density ratio. Consequently, primary fingers in planetary cores are expected to develop only on small spatial scales, on the order of 1 m. Note that an exception may occur close to

the stability boundaries of fingering convection, especially when the stratification is extremely weak at low Rayleigh numbers. In this regime, columnar flows can develop with an azimuthal extent comparable to the layer thickness, as described by Monville et al. (2019); Mather and Simitev (2021); Guervilly (2022). In the limit $Ek \ll 1$, the lower stability boundary occurs at $Ra_c \approx 100Ek^{-1}$ (Monville et al., 2019), corresponding to $N^2/\Omega^2 \approx 10^{-11}$ for Mercury.

Beyond the primary fingering mode, additional large-scale flows emerge depending on the regime. In the range $1 < N^2/\Omega^2 < 100$ and at sufficiently small Ekman numbers, we observe clustering of fingers in the upper domain, where the local density ratio is larger and fingering convection less vigorous. These clusters are associated with weak, large-scale density anomalies and surrounded by toroidal gyres driven by the Coriolis force. These toroidal gyres dominate the local dynamics. They differ from the toroidal jets reported by Tassin et al. (2024), which flow along concentric shells about an arbitrary rotation axis. The size of the density anomalies and associated gyres does not appear to vary significantly with the control parameters, although this cannot be established with certainty from our simulations given that they occur over a limited range of Ra_c and Ek. Their typical azimuthal order is $m \approx 5 - 10$. If their size is indeed insensitive to these parameters, we may infer that such structures would have characteristic horizontal scales of approximately 500 - 1000 km under Mercury's core conditions.

In the intermediate regime $(1 < N^2/\Omega^2 < 10)$, fingering convection exhibits a novel feature: axisymmetric or spiraling bands of poloidal flow confined within the tangent cylinder. These bands form concentric cylindrical structures that are nearly invariant along the rotation axis and slowly drift equatorward. They are highly anisotropic, with latitudinal widths greater than the Stern scale (roughly twice the Stern scale, though their domain of existence is too narrow to confirm this reliably) but azimuthal extents far larger. They grow and saturate over viscous timescales, gradually superseding primary fingering, and contribute to compositional mixing slightly more efficiently than the surviving columnar fingers in the equatorial region. The bands are robustly found within $1 \lesssim N^2/\Omega^2 \lesssim 10$ but do not persist outside this range.

In the rapidly-rotating regime $(N^2/\Omega^2 < 1)$, the mixing is laterally inhomogeneous, initially more vigorous near the equator. This generates latitudinal compositional gradients that are in a thermo-compositional wind balance, analogous to the thermal wind in single-component thermal convection (e.g. Aubert, 2005). The resulting radial shear is disruptive to fingering convection outside the tangent cylinder, weakening the mixing of composition in that region. As N^2/Ω^2 increases, enhanced mixing at higher latitudes leads to a reversal of the latitudinal compositional gradient and, in turn, of the direction of the zonal flow, from retrograde to prograde. The zonal flow amplitude, quantified by the zonal Rossby number Ro_0 , scales linearly with N^2/Ω^2 and reaches a maximum value of $Ro_0 \approx 0.1$ at $N^2/\Omega^2 = 10$. For stronger stratification, the zonal flow gradually diminishes as rotation becomes less influential and the lateral inhomogeneity of the mixing fades.

For rapid rotation at $N^2/\Omega^2 = 0.06$, we obtained a case in which an equatorially-antisymmetric and axisymmetric mode is favoured. This mode corresponds to hemispherical convection, where the fluid in the northern hemisphere is colder and richer in light elements than in the southern hemisphere. The associated equatorially-antisymmetric zonal flow (slower in the northern hemisphere) becomes dominant over the usual equatorially-symmetric zonal flow. This behaviour occurs only for this specific parameter set: the mode decays at smaller stratification and becomes subdominant at larger stratification. It closely resembles the linear mode identified by Monville et al. (2019) in a full-sphere geometry, indicating that it can also arise in a thick spherical shell.

In most of the explored parameter space, we therefore find that fingering convection generates large-scale flows in addition to the primary small-scale fingers. The resulting large-scale dynamics is remarkably diverse, exhibiting axisymmetric bands of poloidal flows, finger clusters, toroidal gyres, hemispherical convection, and zonal flows. Although these flows generally have small local Reynolds numbers (except for the zonal flows), they may possess interesting dynamo properties or interact with ambient magnetic fields in ways that remain to be elucidated.

One property of the small-scale fingers that may be relevant for magnetic interactions is their pronounced radial asymmetry in the regime weakly influenced by rotation $(N^2/\Omega^2 > 10)$, characterized by intense, concentrated upflows surrounded by more diffuse downflows. This asymmetry could enable topological magnetic pumping, as first proposed by Drobyshevski and Yuferev (1974) in the context of the solar interior. In the solar convection zone, compressible convection manifests as narrow downwelling lanes separating broader, weaker upflows; in this configuration, horizontal magnetic fields are expected to be carried downward by the convection (e.g. Tobias et al., 2001). In contrast, the radial asymmetry observed here is reversed, suggesting by analogy that magnetic flux might instead be pumped outward from the stable layer. However, it is unclear whether the degree of radial asymmetry associated with Boussinesq fingering convection would be sufficient for such magnetic flux pumping to operate effectively.

Of perhaps more direct relevance to the role of stable layers in shaping planetary magnetic fields is the spontaneous generation of strong zonal flows, even in the absence of imposed boundary heterogeneity. These zonal flows, and the associated shear, are often invoked as a mechanism to attenuate non-axisymmetric magnetic fields passing through a stable layer, thereby promoting axisymmetrisation of the surface magnetic field (Stevenson, 1982). According to Stevenson (1982)'s linear analysis, achieving a dipole tilt below one degree at Mercury's surface requires $Ro_0 \gtrsim 10^{-4}$ for an 800 km-thick stable layer (see discussion in Guervilly (2022)). Our results suggest zonal flows sufficient to induce effective axisymmetrisation over $N^2/\Omega^2 \in [10^{-2}, 25]$. For stronger stratification, the flows may still generate adequate shear, but further simulations (particularly in Series 2 at fixed $Ek = 10^{-4}$) are needed to confirm this. (Note that in Series 1, where $Ek \to 0$, the Rossby number becomes less meaningful for $N^2/\Omega^2 > 100$.) Ultimately, nonlinear magnetohydrodynamic simulations that include the feedback of the Lorentz force are required to properly test this scenario.

Finally, our results demonstrate that simulations extending over long integration times are essential to capture the rich dynamics of fingering convection: the equatorially-antisymmetric mode observed at $N^2/\Omega^2 = 0.06$ grows and saturates only very slowly, becoming dominant after roughly 60 viscous timescales; similarly, the reversal of zonal flow direction at $N^2/\Omega^2 = 0.2$ occurs only after several tens of viscous timescales; the bands of poloidal flow in the intermediate regime also require several viscous timescales to saturate. As a result, global simulations of fingering convection are computationally demanding, owing to the wide range of spatial and temporal scales involved. This limits our ability to approach realistic core conditions, particularly at low Ekman numbers. For example, in our exploration of the regime $N^2/\Omega^2 > 1$, we were restricted to Ekman numbers $Ek \ge 10^{-4}$, whereas in Mercury's core $Ek \approx 10^{-12}$. It is therefore difficult to determine whether the slow dynamics observed over viscous timescales in our simulations would remain relevant under planetary core conditions, where the characteristic viscous timescales at large scales exceed several billion years. These processes may plausibly evolve on shorter timescales in realistic core regimes, but confirming this would require computationally intensive simulations at lower Ekman numbers.

Acknowledgements

This work was supported by the UK Science and Technology Facilities Council [ST/W001039/1; UKRI1201]. This research used the Rocket High Performance Computing service at Newcastle University and the DiRAC Data Intensive service (CSD3) at the University of Cambridge, managed by the University of Cambridge University Information Services on behalf of the STFC DiRAC HPC Facility (www.dirac.ac.uk). The DiRAC component of CSD3 at Cambridge was funded by BEIS, UKRI and STFC capital funding and STFC operations grants. DiRAC is part of the UKRI Digital Research Infrastructure. For the purpose of open access, the authors have applied a Creative Commons Attribution (CC BY) licence to any Author Accepted Manuscript version arising from this submission.

Data statement

On acceptance of the paper, datasets for this research will be available on the Figshare powered Newcastle University research data repository (https://data.ncl.ac.uk), which creates an identifier (DOI) for each deposit. The numerical code (XSHELLS) used for this research is openly available at https://nschaeff.bitbucket.io/xshells/.

Appendix A. List of simulations

Ek	N^2/Ω^2	(N_r, L_{max}, M_{max})	Re	Re_0	Nu_c
5×10^{-5}	0.016	(192, 120, 110)	2.0	1.8	1.098
$1 \times 10^{-4\dagger}$	0.062	(192, 120, 110)	2.5	3.7	1.108
1.2×10^{-4}	0.090	(192, 120, 110)	2.7	3.8	1.128
1.4×10^{-4}	0.12	(192, 120, 110)	2.8	3.6	1.159
1.5×10^{-4}	0.14	(192, 120, 110)	3.0	3.2	1.174
1.6×10^{-4}	0.16	(192, 120, 110)	3.3	2.6	1.190
$1.8 \times 10^{-4*}$	0.20	(192, 120, 110)	3.5	2.1	1.207
$1.8 \times 10^{-4**}$	0.20	(192, 120, 110)	3.3	6.8	1.159
2×10^{-4}	0.25	(192, 120, 110)	3.0	8.9	1.164
2.5×10^{-4}	0.39	(192, 120, 110)	3.4	13.5	1.170
3×10^{-4}	0.56	(192, 120, 110)	3.3	18.3	1.167
3.33×10^{-4}	0.69	(192, 120, 110)	2.9	21.5	1.162
4×10^{-4}	1.0	(192, 120, 110)	3.1	27.2	1.162
5×10^{-4}	1.6	(192, 120, 110)	3.4	32.5	1.215
6.66×10^{-4}	2.8	(192, 120, 110)	3.6	44.1	1.270
8×10^{-4}	4.0	(192, 120, 110)	3.8	43.7	1.322
1×10^{-3}	6.2	(192, 120, 110)	4.0	42.3	1.378
2×10^{-3}	24.9	(192, 120, 110)	4.9	24.7	1.530
4×10^{-3}	99.6	(192, 120, 110)	5.5	13.1	1.649
6×10^{-3}	224	(192, 120, 110)	5.6	8.6	1.702
8×10^{-3}	398	(192, 120, 110)	5.7	6.3	1.731
1×10^{-2}	623	(192, 120, 110)	5.7	5.2	1.754
3.33×10^{-2}	6902	(192, 120, 110)	5.6	2.0	1.827
6.66×10^{-2}	27619	(192, 120, 110)	5.5	1.3	1.754
1×10^{-1}	62240	(192, 120, 110)	5.4	1.0	1.873

Table A.1: Simulations from Series 1 with constant $Ra_c = 2 \times 10^7$, $Ra_t = -Ra_c/3$ and Le = 10. The numerical resolution is given by the number of radial points, N_r , and the truncation degree and order of the spherical harmonics decomposition, L_{max} and M_{max} . Re is the Reynolds number for the poloidal flow, Re_0 the Reynolds number for the zonal flow. (†) For $Ek = 10^{-4}$, the output quantities are calculated before the transition in the equatorial symmetry (see Table A.2). (*) – (**) The output quantities for the simulation at $Ek = 1.8 \times 10^{-4}$ averaged before (after) the reversal of the direction of the zonal velocity are denoted by * (** respectively).

Ra_c	N^2/Ω^2	(N_r, L_{max}, M_{max})	Re	Re_0	Nu_c
$2 \times 10^{7\dagger}$	0.062	(192, 163, 163)	2.5	3.8	1.105
$2 \times 10^{7\dagger\dagger}$	0.062	(192, 163, 163)	2.3	4.6	1.107
4×10^{7}	0.12	(220, 163, 163)	4.0	3.5	1.196
6×10^{7}	0.19	(250, 180, 160)	4.3	15.3	1.175
8×10^{7}	0.25	(250, 180, 160)	4.7	24.2	1.179
1.2×10^{8}	0.37	(250, 180, 160)	5.1	41.6	1.172
2×10^{8}	0.62	(300, 200, 180)	6.1	83.4	1.194
4×10^{8}	1.2	(300, 220, 220)	6.9	182.9	1.250
8×10^{8}	2.5	(300, 220, 220)	8.5	303.8	1.346
1.2×10^9	3.7	(300, 240, 220)	10.2	360.8	1.369
1.6×10^9	5.0	(300, 240, 220)	11.5	391.0	1.397
2.4×10^{9}	7.5	(300, 240, 220)	13.7	402.6	1.431
4×10^{9}	12.4	(504, 380, 255)	17.9	309.2	1.511
8×10^{9}	24.9	(608, 485, 340)	23.4	238.4	1.572

Table A.2: Simulations from Series 2 with constant $Ek = 10^{-4}$, $Ra_t = -Ra_c/3$ and Le = 10. (†) – (††) The output quantities for the simulation at $Ra_c = 2 \times 10^7$ averaged before (after) the transition in the flow equatorial symmetry are denoted by † (†† respectively).

References

Anderson, B.J., Johnson, C.L., Korth, H., Winslow, R.M., Borovsky, J.E., Purucker, M.E., Slavin, J.A., Solomon, S.C., Zuber, M.T., McNutt, R.L., 2012. Low-degree structure in Mercury's planetary magnetic field. J. Geophys. Res.: Planets 117.

Aubert, J., 2005. Steady zonal flows in spherical shell dynamos. J. Fluid Mech. 542, 53-67.

Baines, P., Gill, A., 1969. On thermohaline convection with linear gradients. J. Fluid Mech. 37, 289-306.

Bouffard, M., Labrosse, S., Choblet, G., Fournier, A., Aubert, J., Tackley, P.J., 2017. A particle-in-cell method for studying double-diffusive convection in the liquid layers of planetary interiors. J. Comp. Physics 346, 552–571.

Brown, J.M., Garaud, P., Stellmach, S., 2013. Chemical transport and spontaneous layer formation in fingering convection in astrophysics. Astrophys. J. 768, 34.

Christensen, U.R., 2006. A deep dynamo generating Mercury's magnetic field. Nature 444, 1056-1058.

Christensen, U.R., Wicht, J., 2008. Models of magnetic field generation in partly stable planetary cores: Applications to Mercury and Saturn. Icarus 196, 16–34.

Davies, C.J., Pommier, A., Greenwood, S., Wilson, A., 2024. Thermal and magnetic evolution of Mercury with a layered Fe-Si (-S) core. Earth Planet. Sci. Lett. 641, 118812.

Drobyshevski, E., Yuferev, V., 1974. Topological pumping of magnetic flux by three-dimensional convection. J. Fluid Mech. 65, 33–44.

Dumberry, M., Rivoldini, A., 2015. Mercury's inner core size and core-crystallization regime. Icarus 248, 254–268.

Fraser, A.E., Reifenstein, S.A., Garaud, P., 2024. Magnetized fingering convection in stars. Astrophys. J. 964, 184.

Garaud, P., 2018. Double-diffusive convection at low Prandtl number. Ann. Rev. Fluid Mech. 50, 275-298.

Garaud, P., 2021. Journey to the center of stars: the realm of low Prandtl number fluid dynamics. Phys. Rev. Fluids 6, 030501.

- Gastine, T., Aurnou, J.M., 2023. Latitudinal regionalization of rotating spherical shell convection. J. Fluid Mech. 954, R1.
- Greenwood, S., Davies, C.J., Mound, J.E., 2021. On the evolution of thermally stratified layers at the top of Earth's core. Phys. Earth Planet. Int. 318, 106763.
- Grossmann, S., Lohse, D., 2000. Scaling in thermal convection: a unifying theory. J. Fluid Mech. 407, 27–56.
- Guervilly, C., 2022. Fingering convection in the stably stratified layers of planetary cores. J. Geophys. Res.: Planets 127, e2022JE007350.
- Hage, E., Tilgner, A., 2010. High Rayleigh number convection with double diffusive fingers. Phys. Fluids 22.
- Hansen, U., Yuen, D.A., 1990. Nonlinear physics of double-diffusive convection in geological systems. Earth-Science Reviews 29, 385–399.
- Harrington, P., Garaud, P., 2019. Enhanced mixing in magnetized fingering convection, and implications for red giant branch stars. Astrophys. J. Lett. 870, L5.
- Hauck, S.A., Aurnou, J.M., Dombard, A.J., 2006. Sulfur's impact on core evolution and magnetic field generation on Ganymede. J. Geophys. Res. Planets 111.
- Kellner, M., Tilgner, A., 2014. Transition to finger convection in double-diffusive convection. Phys. Fluids 26.
- Knibbe, J.S., Rivoldini, A., Zhao, Y., Van Hoolst, T., 2025. On the thermal evolution and magnetic field generation of planet Mercury. Phys. Earth Planet. Int. 363, 107348.
- Kolhey, P., Heyner, D., Wicht, J., Gastine, T., Glassmeier, K.H., Plaschke, F., 2025. Dynamo models with a Mercury-like magnetic offset dipole. J. Geophys. Res. Planets 130, e2024JE008660.
- Kunze, E., 2003. A review of oceanic salt-fingering theory. Progress in Oceanography 56, 399–417.
- Manglik, A., Wicht, J., Christensen, U., 2010. A dynamo model with double diffusive convection for Mercury's core. Earth Plant. Sci. Lett. 289, 619–628.
- Mather, J.F., Simitev, R.D., 2021. Regimes of thermo-compositional convection and related dynamos in rotating spherical shells. Geophys. Astrophys. Fluid Dyn. 115, 61–84.
- Monville, R., Vidal, J., Cébron, D., Schaeffer, N., 2019. Rotating double-diffusive convection in stably stratified planetary cores. Geophys. J. Int. 219, 195–218.
- Mound, J.E., Davies, C.J., 2017. Heat transfer in rapidly rotating convection with heterogeneous thermal boundary conditions. J. Fluid Mech. 828, 601–629.
- Net, M., Garcia, F., Sánchez, J., 2012. Numerical study of the onset of thermosolutal convection in rotating spherical shells. Phys. Fluids 24, 064101.
- Paparella, F., Von Hardenberg, J., 2012. Clustering of salt fingers in double-diffusive convection leads to staircaselike stratification. Phys. Rev. Lett. 109, 014502.
- Radko, T., 2013. Double-diffusive convection. Cambridge University Press.
- Radko, T., Smith, D.P., 2012. Equilibrium transport in double-diffusive convection. J. Fluid Mech. 692, 5–27.
- Radko, T., Stern, M.E., 2000. Finite-amplitude salt fingers in a vertically bounded layer. J. Fluid Mech. 425, 133–160.
- Schaeffer, N., 2013. Efficient spherical harmonic transforms aimed at pseudospectral numerical simulations. Geochem, Geophys, Geosyst. 14, 751–758.

- Schaeffer, N., Jault, D., Nataf, H.C., Fournier, A., 2017. Turbulent geodynamo simulations: a leap towards Earth's core. GJI 211, 1–29.
- Schmitt, R.W., 1979. The growth rate of super-critical salt fingers. Deep Sea Research Part A. Oceanographic Research Papers 26, 23–40.
- Schmitt, R.W., 1994. Double diffusion in oceanography. Ann. Rev. Fluid Mech. 26, 255–285.
- Schmitt, R.W., 2011. Thermohaline convection at density ratios below one: A new regime for salt fingers. J. Marine Res. 69, 779–795.
- Sengupta, S., Garaud, P., 2018. The effect of rotation on fingering convection in stellar interiors. Astrophys. J. 862, 136.
- Silva, L., Mather, J.F., Simitev, R.D., 2019. The onset of thermo-compositional convection in rotating spherical shells. Geophys. Astrophys. Fluid Dyn. 113, 377–404.
- Sparks, R.S.J., Huppert, H.E., Turner, J.S., 1984. The fluid dynamics of evolving magma chambers. Phil. Trans. Royal Soc. London. Series A 310, 511–534.
- Stanley, S., Mohammadi, A., 2008. Effects of an outer thin stably stratified layer on planetary dynamos. Phys. Earth Planet. Int. 168, 179–190.
- Stellmach, S., Traxler, A., Garaud, P., Brummell, N., Radko, T., 2011. Dynamics of fingering convection. Part 2 The formation of thermohaline staircases. J. Fluid Mech. 677, 554–571.
- Stern, M.E., 1960. The "salt-fountain" and thermohaline convection. Tellus 12, 172–175.
- Stevenson, D.J., 1982. Reducing the non-axisymmetry of a planetary dynamo and an application to Saturn. Geophys. Astrophys. Fluid Dyn. 21, 113–127.
- Takahashi, F., Shimizu, H., Tsunakawa, H., 2019. Mercury's anomalous magnetic field caused by a symmetry-breaking self-regulating dynamo. Nature communications 10, 1–8.
- Tassin, T., Gastine, T., Fournier, A., 2024. Fingering convection in a spherical shell. J. Fluid Mecha. 988, A18.
- Tian, Z., Zuber, M., Stanley, S., 2015. Magnetic field modeling for Mercury using dynamo models with a stable layer and laterally variable heat flux. Icarus 260, 263–268.
- Tobias, S.M., Brummell, N.H., Clune, T.L., Toomre, J., 2001. Transport and storage of magnetic field by overshooting turbulent compressible convection. The Astrophysical Journal 549, 1183.
- Traxler, A., Garaud, P., Stellmach, S., 2011a. Numerically determined transport laws for fingering ("thermohaline") convection in astrophysics. Astrophys. J. Lett. 728, L29.
- Traxler, A., Stellmach, S., Garaud, P., Radko, T., Brummell, N., 2011b. Dynamics of fingering convection. Part 1 Small-scale fluxes and large-scale instabilities. J. Fluid Mech. 677, 530–553.
- Turner, J., 1967. Salt fingers across a density interface. Deep-Sea Res. 14, 599-611.
- Vilim, R., Stanley, S., Hauck, S., 2010. Iron snow zones as a mechanism for generating Mercury's weak observed magnetic field. J. Geophys. Res.: Planets 115.
- Wardinski, I., Amit, H., Langlais, B., Thébault, E., 2021. The internal structure of Mercury's core inferred from magnetic observations. J. Geophys. Res. Planets 126, e2020JE006792.
- Wicht, J., Heyner, D., 2014. Mercury's magnetic field in the Messenger era. Planetary Geodesy and Remote Sensing 10, 223–262.

- Yang, Y., Van Der Poel, E.P., Ostilla-Mónico, R., Sun, C., Verzicco, R., Grossmann, S., Lohse, D., 2015. Salinity transfer in bounded double diffusive convection. J. Fluid Mech. 768, 476–491.
- Yang, Y., Verzicco, R., Lohse, D., 2016. Scaling laws and flow structures of double diffusive convection in the finger regime. J. Fluid Mech. 802, 667–689.